Human iPSC-derived cerebral organoids model features of Leigh Syndrome and reveal abnormal corticogenesis

Alejandra I. Romero-Morales[1], Anuj Rastogi[1], Hoor Temuri[1], Megan L. Rasmussen[1], Gregory Scott McElroy[3], Lawrence Hsu[2], Paula M. Almonacid[4], Bryan A. Millis[1], Navdeep S. Chandel[3,5], Jean-Philippe Cartailler[2] and Vivian Gama[1,2,6]

[1]Vanderbilt University, Cell and Developmental Biology, Nashville, TN.
[2]Vanderbilt University, Creative Data Solutions, Vanderbilt Center for Stem Cell Biology, Nashville, TN
[3]Northwestern University, Feinberg School of Medicine Department of Medicine Division of Pulmonary and Critical Care Medicine, Chicago, IL
[4]Universidad EAFIT, School of Economics and Finances, Colombia
[5]Northwestern University, Feinberg School of Medicine Department of Biochemistry and Molecular Genetics, Chicago, IL
[6]Vanderbilt University, Vanderbilt Brain Institute, Nashville, TN

Corresponding author

Correspondence should be addressed to:

Vivian Gama
PMB407935
465 21st Avenue South, 4150A
Vanderbilt University
Nashville, TN 37240-7935
Tel: (615) 875-9490
vivian.gama@vanderbilt.edu

Running title: Modeling the effect of Leigh syndrome-associated mutations using human cerebral organoids

Keywords: Leigh syndrome, stem cells, glycolysis, oxidative phosphorylation, mitochondria, neural precursor cells, neural rosettes, brain organoids

Summary

Leigh syndrome (LS) is a rare, inherited neuro-metabolic disorder that presents with bilateral brain lesions. This disease is caused by defects in the mitochondrial respiratory chain and associated nuclear-encoded proteins. We generated induced pluripotent stem cells (iPSCs) from three widely available LS fibroblast lines and identified, through whole exome and mitochondrial sequencing, unreported mutations in pyruvate dehydrogenase (GM0372, PDH; GM13411, MT-ATP6/PDH) and dihydrolipoyl dehydrogenase (GM01503, DLD). LS derived cell lines were viable and able to differentiate into key progenitor populations, but we identified several abnormalities in three-dimensional differentiation models of brain development. The DLD-mutant line showed decreased neural rosette (NR) formation, and there were differences in NR lumen area in all three LS lines compared to control. LS-derived cerebral organoids showed defects in neural epithelial bud generation and reduced size when grown for 100 days. Loss of cortical architecture and markers were detected at days 30 and 100. The MT-ATP6/PDH line produced organoid neural progenitor cells with an abnormal mitochondrial morphology characterized by fragmentation and disorganization, and demonstrated increased generation of astrocytes. These studies aim to provide a comprehensive phenotypic characterization of available patient-derived cell lines that could be used as LS model systems.

Introduction

Leigh syndrome (LS), or sub-acute necrotizing encephalomyelopathy, is an inherited neuro-metabolic disorder that affects the central nervous system (CNS) (Baertling et al., 2014; Gerards et al., 2016; Leigh, 1951; Sorbi and Blass, 1982). LS is a rare, progressive, early-onset disease with a prevalence of 1 in 40,000 live births (Lake et al., 2016). The pathologic features of LS are focal, bilateral lesions in one or more areas of the CNS, including the brainstem, thalamus, basal ganglia, cerebellum, and spinal cord. The most common underlying cause is defective oxidative phosphorylation (OXPHOS), due to mutations in genes encoding complexes of the mitochondrial respiratory chain (Baertling et al., 2014; Lake et al., 2015, 2016). The LS phenotype caused by mitochondrial-encoded gene mutations can be rescued by mitochondrial replacement, highlighting the importance of this organelle in LS disease progression (Ma et al., 2015).

The availability of animal models and brain tissue from biopsies has provided critical insight into this disease. However, our understanding of the etiology and pathology of complex neurological diseases like LS would benefit from human-derived platforms such as an induced pluripotent stem cell- derived model (Quadrato et al., 2016). The ability to reprogram somatic cells into induced pluripotent stem cells (iPSCs), followed by differentiation into specific lineages has become an useful tool for complex disease modeling (Kelava and Lancaster, 2016; Di Lullo and Kriegstein, 2017). In the context of LS, iPSCs have been successfully generated from patients with mutations in Mitochondrially Encoded ATP Synthase Membrane Subunit 6 (MT-ATP6) (Galera-Monge et al., 2016; Grace et al., 2019; Lorenz et al., 2017; Ma et al., 2015), Mitochondrially Encoded NADH:Ubiquinone Oxidoreductase Core Subunit 3 (MT-ND3) subunit (Hattori et al., 2016) and the nuclear encoded gene Surfeit locus protein 1 (SURF1) (Inak et al., 2019). These iPSC-model systems have been proposed for drug discovery (Inak et al., 2017; Lorenz et al., 2017) as well as testing platforms for potential metabolic rescue treatments (Ma et al., 2015).

Many studies have used LS patient fibroblasts commercially available at the Coriell Institute. This repository provides scientists around the world with resources for cell and genetic research. Here we report our findings on the genomic and phenotypic characterization of iPSCs derived from three LS fibroblast lines available at Coriell. Whole exome and mitochondrial sequencing revealed previously unidentified mutations in these patient-derived cell lines. While these LS mutations had no effects on pluripotency, trilineage differentiation, or apoptotic sensitivity, three-dimensional differentiation into neural rosettes and cerebral organoids resulted in severe abnormalities. LS-iPSC-derived 100-day cerebral organoids showed decreased size as well as defects in the generation of neural epithelial buds. Corticogenesis was impaired in all LS mutant cell lines. MT-ATP6/PDH showed a decrease in NPC and cortical plate markers at day 30, while DLD and PDH mutants showed a reduction of the upper layer markers SATB2, BRN2 and CUX1 at day 100. These results point to aberrant corticogenesis as a driver of LS pathogenesis and demonstrate the utility of iPSC-derived systems to recapitulate CNS phenotypes and to test potential strategies to restore neurogenesis in LS.

Results

Genomic characterization of Leigh syndrome fibroblasts.

Due to the limited genomic information available for the three cell lines, we performed whole exome sequencing (WES) and mitochondrial sequencing of the fibroblasts prior to reprogramming (Figure 1A-C). Targeted analysis of the genes associated with Leigh syndrome (Lake et al., 2016) revealed a loss of function insertion/deletion (indel) frame shift in pyruvate dehydrogenase complex (PDHc) E1 alpha 1 subunit or pyruvate dehydrogenase (PDHA1, c.79delC, p.Arg27fs) in the cell lines GM03672 and GM13411. A single-nucleotide polymorphism (SNP) in the PDHc E3 subunit or dihydrolipoyl dehydrogenase (DLD, c.100A>G, p.Thr34Ala) was identified in GM01503 (Table S1). In addition to being part of the PDHc, DLD is also a component of the α-ketoglutarate and branched chain α-ketoacid dehydrogenase complexes (Craigen, 1996). Despite

the lack of genomic data, dysfunction of the PDH complex had been previously suggested in GM03672 and GM01503 (Hinman et al., 1989; Huh et al., 1990; Sorbi and Blass, 1982) as the main driver of the disease in these patients. To our knowledge, mutations in the nuclear genome of GM13411 have not been reported to date.

Mitochondrial sequencing identified several SNPs in all of the cell lines (Figure 1D). A loss of function SNP in the MT-ATP6 gene was identified in the GM13411 line. These mutations were reported in the original clinical case (Pastores et al., 1994). The authors described the T to G transition at the 8993 position that results in the substitution of a highly conserved leucine residue for an arginine (L156R). MT-ATP6 is part of the F0 domain of ATP synthase that functions as a proton channel. The L156R substitution prevents the induction of c-ring rotation, resulting in decreased ATP synthesis (Uittenbogaard et al., 2018). Heteroplasmic analysis of fibroblasts showed a 92% frequency of this mutation in the cell population, which is consistent with previous reports (Galera-Monge et al., 2016; Iyer et al., 2012; Pastores et al., 1994).

Characterization of iPSCs derived from commercially available Leigh syndrome fibroblasts.

Metabolic remodeling is a crucial step toward reprogramming of somatic cells into iPSCs (Mathieu and Ruohola-Baker, 2017; Panopoulos et al., 2012; Rasmussen and Gama, 2020; Rastogi et al., 2019; Wu et al., 2016). Reprogramming of fibroblasts was performed as previously described (Takahashi et al., 2007) (Figure S1A); we generated iPSCs from a healthy age-matched control and the three LS cell lines. Pluripotency was evaluated using the microarray based analysis PluriTest (Müller et al., 2011). All three LS cell lines showed a high pluripotency score and a low novelty score (Figure S1B-C), congruent with the transcriptional profile of pluripotent stem cells. Moreover, all the reprogrammed cells expressed the pluripotent markers *NANOG* and *OCT4* (Figure S1D) and had a normal karyotype (Figure S1E)

To assess the ability of the LS and control cell lines to differentiate into the three germ layers, we performed trilineage differentiation. Commitment into ectodermal fate was evaluated by immunofluorescence staining of the marker PAX6 (Figure 2A), as well as the mRNA expression of the genes *GATA3* and *PAX6* (Figure 2B). The endoderm lineage was assessed by protein expression of the marker SOX17 (Figure 2C) and by qPCR with the expression of the genes *CDX2* and *SOX17* (Figure 2D). The PDH mutant cell line showed increased expression of the endodermal gene SOX17 (Figure 2D) compared to control and the other LS cell lines. Clinical data available from the patient with the PDH mutation showed elevated blood pyruvate levels. High concentrations of pyruvate have been shown to potentiate the differentiation of human embryonic stem cells (hESCs) into endodermal and mesodermal lineages while suppressing the expression of ectodermal markers in a lineage specific fashion (Song et al., 2019). Finally, mesodermal lineage was confirmed by the staining of the protein markers Brachyury and CXCR4 (Figure 2E) and the expression of the genes *TBXT* and *NCAM* (Figure 2F).

Two-dimensional neural differentiation is not affected by Leigh syndrome associated mutations.

To determine if the LS mutations impact the commitment and development of the neural lineage, neural progenitor cells (NPCs) were generated by a dual SMAD inhibition protocol (Chambers et al., 2009) (Figure 3A). NPCs showed expected expression of the neural markers PAX6, NESTIN, and SOX2 (Figure 3B), with no differences between the protein expression of the LS cell lines and control (Figure S2A). The multipotent capacity of NPCs to generate the three basic neural lineages (neurons, astrocytes, and oligodendrocytes) was evaluated using standard protocols (Chambers et al., 2009; TCW et al., 2017; Vescovi and Snyder, 1999). Immunostaining showed β3 TUBULIN-positive neurons, OLIG2-positive oligodendrocytes and S100β-positive astrocytes (Figure 3C). Thus, LS NPCs constitute a multipotent population capable of differentiation into the main cellular populations of the nervous system.

Considering that neural cell death is a hallmark of LS, we performed a cell viability assay to investigate the sensitivity of the LS derived NPCs to different apoptotic stimuli (Figure S2B). Treatment with DNA damaging agents etoposide and neocarzinostatin, as well as the microtubule depolymerizing agent nocodazole, did not show increased sensitivity to cell death in LS NPCs compared to control. To evaluate the susceptibility of the NPCs to mitochondrial damage, we treated these cells with the mitochondrial oxidative phosphorylation uncoupler, CCCP. No difference was observed in the viability of the LS NPCs compared to control treated with this mitochondrial toxicant.

Mitochondria in murine NPCs form an elongated network (Khacho et al., 2016) which fragments as cells differentiate. Characterization of the mitochondrial network using structured illumination microscopy (SIM) showed no major morphological changes in LS NPCs (Figure 3D). Thus, LS mutations do not affect the capacity of the NPCs to further differentiate into the three neural lineages, do not affect the viability of the NPCs when exposed to different exogenous stressors in a monolayer culture, and do not perturb the morphology of the mitochondrial network in these cells.

LS mutations cause differential accumulation of metabolites in neuralized embryoid bodies.

Previous studies using cells from LS patients carrying homozygous *SURF1* (c.769G>A and c.530T>G) (Inak et al., 2019) and MT-ATP6 (m.9185T>C) (Lorenz et al., 2017) mutations showed abnormal generation of neural lineages *in vitro* using two-dimensional culture systems. SURF1 mutations caused impaired neurogenesis in cerebral organoids (Inak et al., 2019). Therefore, we investigated the effects of the PDH, DLD, and MT-ATP6/PDH LS mutations on neurogenesis using three-dimensional (3D) models of neural development as described previously (Lancaster and Knoblich, 2014; Romero-Morales et al., 2019). Most of these 3D neural systems start with the formation of neuralized embryoid bodies (EBs). EBs are generated from a single cell

198 suspension (Itskovitz-Eldor et al., 2000) plated in ultra-low attachment microwells with neural
199 induction media (Figure 4A). EB diameter was measured at day 5 before plating on Matrigel
200 coated imaging plates. All three LS mutant lines showed an increase in their diameter compared
201 to control (Figure 4B, PDH vs Control & DLD vs Control: $p<0.0001$, MT-ATP6/PDH vs Control:
202 $p=0.0209$).

203 We then measured metabolite levels in EBs derived from LS cell lines using LC-MS-based
204 metabolomics (Table S2). Several pathways were found to be potentially altered in the LS EBs
205 compared to controls (Figure 4C and Table S3). These include central carbon metabolism (for
206 example glycolytic intermediates like Fructose 2,6-bisphosphate (f2,6p) and tricarboxylic acid
207 cycle (TCA) intermediates like citrate seem to be consistently enriched), glutathione metabolism,
208 serine metabolism, cysteine metabolism, and nucleotide metabolism. Dihydroorotate, lactate, and
209 aspartate are metabolites that were altered in the setting of electron transport chain (ETC)
210 inhibition, and there is evidence of a trend towards enrichment of dihydroorotate, lactate, and
211 aspartate compared to control. There also appears to be an enrichment of the NAD pool. These
212 results suggest that LS mutations result in differential changes in metabolite concentrations, which
213 may cause downstream changes in gene expression or cellular function.

214

215 **Neural rosettes derived from Leigh syndrome iPSCs show morphological differences.**

216 To investigate the effects of LS associated mutations in early stages of CNS development,
217 we generated neural rosettes using EBs grown in the presence of SMAD inhibitor media (Figure
218 5A) (Elkabetz et al., 2008; Zhang et al., 2001). These structures have previously been established
219 to recapitulate the early neural tube formation stage of development (Elkabetz et al., 2008; Wilson
220 and Stice, 2006).

221 Neural rosettes were stained with the tight junction marker ZO-1 (Elkabetz et al., 2008;
222 Hříbková et al., 2018) and the centrosomal marker CDK5RAP2 (Figure 5B). Quantification of the
223 number of neural rosettes per field of view showed a reduction in the counts of these structures

in the DLD mutant compared to controls (Figure 5C, $p<0.001$). Lumen area quantification showed an increase in the PDH and MT-ATP6/PDH mutants, while the DLD mutant line showed a decrease in their area relative to controls (Figure 5D). The neural rosettes obtained from all cell lines followed the expected formation sequence described previously (Hříbková et al., 2018). The polymerization of α-tubulin and the generation of the ZO-1 ring at the apical region of the rosettes are conserved in the LS mutants. Increased neural rosette lumen size has previously been associated with TGFβ pathway activation (Medelnik et al., 2018), Notch and SHH pathway activation, and WNT inhibition (Elkabetz et al., 2008). Large rosette formation has been previously shown to be a consequence of apical domain opening and expansion rather than a process dependent on cell proliferation (Medelnik et al., 2018).

Leigh syndrome associated mutations disrupt corticogenesis in cerebral organoids.

To investigate the effects of these mutations during corticogenesis, we generated cerebral organoids from LS iPSCs (Figure 6A). Differences between the cell lines became apparent as early as the neuroepithelial bud expansion phase. After Matrigel embedding, the MT-ATP6/PDH mutant cell line showed poor budding with large areas of non-neuroepithelial cells (Figure S3A). Defective organoid formation in this cell line was significantly higher than control and the other two LS cell lines (Figure S3B). A previous report showed that when iPSCs generated from fibroblasts harboring the same T8993G mitochondrial mutation were differentiated into EBs, there was rapid regression and death after 7 days in suspension, while the monolayer culture did not show obvious deficits in cell growth (Grace et al., 2019). Given the fact the neuroectoderm expansion phase happens during days 7-10, the degeneration of the MT-ATP6/PDH organoids after embedding may recapitulate these previously reported observations.

Higher metabolic requirements have been shown to be associated with NPC proliferation and migration in three-dimensional scaffolds and development (Fang et al., 2020; Homem et al., 2015). As the PDH mutant line did not show this particular phenotype during the expansion of the

neural epithelium, the presence of the additional mitochondrial mutation in the MT-ATP6/PDH line and the metabolic burden generated by the double mutation may be the reason for reduction of organoid formation efficiency.

Cerebral organoid growth was tracked for 100 days (Figure 6B). Growth differences in the average diameter of the organoids become significant at day 80 between control and the PDH mutant line. At days 90 and 100, organoids derived from all LS cell lines were significantly smaller than the controls. Phenotypic information available for the patient from which the PDH mutant cell line was derived indicate that this particular patient presented with microcephaly. Hence, we were able to mimic an aspect of the patient phenotype *in vitro* using the cerebral organoid model system.

In order to assess the effect of the LS mutations during the first stages of corticogenesis, day 30 organoids were sectioned and stained for ventricular zone (VZ), subventricular zone (sVZ), and cortical plate (CP) markers (Figure 6C). As expected, based on the defective neuroepithelial expansion, MT-ATP6/PDH organoids showed a significant reduction in the number of cells that stained positive for the NPC markers PAX6 and NESTIN, as well as the outer radial glia marker TBR2 (Figure 6D). In addition to these findings, the overall architecture in MT-ATP6/PDH organoids was compromised. There were few to no ventricle-like structures present and the foci of PAX6+ cells were not organized in the expected radial pattern.

Migration of early born neurons *in vivo* depends on pioneer Cajal-Retzius neurons that are positive for the glycoprotein REELIN (Lancaster et al., 2017). Cells positive for this marker were identified in superficial regions of control, PDH, and DLD organoids, while none were observed in the MT-ATP6/PDH organoids (Figure 6E). Early born neurons at this time point are expected to migrate into the CP that will later give rise to the deep cortical layers (Camp et al., 2015). CTIP2+ and TBR1+ cells were observed in control, PDH, and DLD organoids but absent in MT-ATP6/PDH organoids, demonstrating once again a profound impairment in the early stages of corticogenesis when both MT-ATP6 and PDH mutations are present.

Mitochondrial morphology was evaluated in the VZ NPCs of the cerebral organoids. Cells positive for NPC marker SOX2+ demonstrated elongated mitochondrial networks that extend radially from the ventricle-like lumen (Figure 6F). This observation is consistent with what has been previously reported in SOX2+ cells in the developing mouse cortex (Khacho et al., 2016). DLD mutant organoid NPCs showed a fragmented mitochondrial network in comparison with control and PDH. As mentioned earlier, the stereotypical arrangement of the VZ was compromised in most MT-ATP6/PDH organoids. In the few areas where ventricle-like structures were identified with a conserved SOX2+ VZ, the mitochondrial network seemed more fragmented and aggregated. This morphology was also observed in the clusters of SOX2+ cells that were scattered throughout the organoid.

In order to assess the proper cortical layer fate specification during normal cortical development, we grew the cerebral organoids until day 100 and probed for upper cortical layer markers (Figure 7A) (Florio and Huttner, 2014; Lui et al., 2011; Saito et al., 2011). Late born superficial layer markers CUX1, BRN2, and SATB2 (layers II, III and IV, respectively) were reduced in PDH and DLD organoids and were absent in MT-ATP6/PDH organoids (Figure 7B-D). CTIP2+ cells were also reduced in PDH and DLD organoids (Figure 7B-C). Interestingly, at day 100, few PAX6+ cells were observed in PDH and DLD organoids, whereas in MT-ATP6/PDH organoids they were present. The reduction in the number and variety of cell types found in PDH and DLD may explain the decrease in the diameter of the organoids derived from these cell lines (Figure 6B).

Compared to controls, LS cerebral organoids showed increased staining for the astrocyte marker S100β at day 100 (Figure 7C). The decrease in the diversity of neuronal cell types and the increase in the presence of S100β+ cells may suggest a switch to astrocyte fate during cortical development in LS. Clinical data from LS patients include a marked gliosis as part of the characteristic findings (Lake et al., 2015). While this marked gliosis is potentially associated with a reactive process secondary to neuronal damage, an intriguing alternate possibility is that

progenitor cells may have an increased propensity to differentiate down the astrocyte lineage due to LS-causative mutations. Previous studies have shown that reactive astrocytes acquire molecular hallmarks of radial glial cells. It was also shown through genetic fate mapping mature astroglial cells can dedifferentiate and resume proliferation (Robel et al., 2009, 2011). Thus, the phenotypes uncovered here could either reflect that chronic metabolic stress induced by Leigh syndrome mutations activates a brain injury response, or that the inhibition of mitochondrial metabolism in neural progenitor cells could cause defects in lineage selection.

We then explored the changes in metabolites in Day 40 organoids from control and LS samples (Figure S4). From the top 10 metabolites identified, the organic osmolyte betaine was increase in the control compared to the DLD and PDH samples and the quaternary amine carnitine was increased in the control compared with all LS samples. L-Carnitine is essential for the transport of long chain fatty acids into mitochondria for degradation by β-oxidation (Jernberg et al., 2017). Carnitine concentration in the brain increases during gestation (Nakano et al., 1989) and has been reported as a therapeutic option for children affected by metabolic diseases. Moreover, this compound has been shown to decrease oxidative stress, improve the brain energy status, and prevent neuronal cell death in animal models of brain injury and ischemia (Ferreira and McKenna, 2017).

Pseudouridine, an isomer of uridine and the most abundant RNA modification, was decreased in DLD organoids. Pseudouridine and pseudouridine synthases (Pus) have been associated with regulating neuronal functions (Angelova et al., 2018). Specifically, Pus3 has been implicated in neural development (Diez-Roux et al., 2011). A truncated form of Pus3 accompanied with reduced levels of pseudouridine in tRNA has been identified in patients with intellectual disabilities (Shaheen et al., 2016).

High lactate was identified in both PDH and MT-ATP6/PDH organoids, correlating with the available clinical information that both patients presented elevated lactic acid in blood (Table 1). Lactic acid accumulation in blood and cerebrospinal fluid is the key clinical indicator for LS

diagnosis and is particularly expected in the setting of PDH dysfunction (Miyabayashi et al., 1985). Also, in these two lines the metabolite proline was elevated. High levels of proline have been associated with negative effects in brain function by interference in glutamatergic neurotransmission (Gogos et al., 1999; Vorstman et al., 2009). In addition, hydroxyphenyllactic acid was elevated in PDH mutant organoids. High levels of this metabolite have been reported in association with high lactate and pyruvate in pediatric lactic acidosis in patients with PDHc deficiency (Stern, 1994). Not surprisingly, in the MT-ATP6/PDH mutant organoids, pyruvate was also increased, correlating with the lactic acidosis expected in the organoids based on the patient phenotypes and the presence of the PDH mutation that hinders flux from pyruvate into the TCA cycle through acetyl-CoA.

Besides the previously mentioned metabolites, MT-ATP6/PDH mutant organoids presented increased levels of choline, cytidine, and leucine. Choline is a crucial metabolite for normal CNS development. Neural tube defects have been associated with lack of choline during early pregnancy (Zeisel, 2006). It has also been shown to increase cell proliferation and decrease apoptosis in fetal rat hippocampal progenitor cells (Albright et al., 1999b, 1999a; Zeisel and Niculescu, 2006). Choline is also crucial for the production of the neurotransmitter acetylcholine, the sphingolipid sphingomyelin, and myelin (Oshida et al., 2003). Concomitantly, cytidine is used with choline for the generation of cytidine-5-diphosphocholine, a crucial intermediate in the biosynthesis of the cell membrane phospholipids phosphatidylcholine and phosphatidylethanolamine (Cansev, 2006; Rema et al., 2008). Increased abundance of the branched chain amino acid leucine has been associated with the metabolic illness maple syrup urine disease and can be extremely neurotoxic (Bridi et al., 2005; García-Cazorla et al., 2014). This amino acid is considered ketogenic as its end products can enter the TCA cycle for energy generation or act as precursors for lipogenesis and ketone body production (Manoli and Venditti, 2016).

Considering all the aforementioned findings, the cerebral organoid system emerges as a promising model for the study of the effects of LS associated mutations in brain development and the effects of metabolic impairment during corticogenesis.

Discussion

Inborn errors of metabolism are rare genetic disorders resulting from defects in metabolic pathways (Agana et al., 2018; Das et al., 2010). Mitochondrial diseases are the most common group of inherited metabolic disorders and are among the most common forms of inherited neurological disorders (Gorman et al., 2016). These illnesses are challenging not only at the time of diagnosis but also during their medical evolution, as they involve multiple organ systems and there are limited therapeutic options (Grier et al., 2018; Parikh et al., 2017; Schaefer et al., 2019).

Leigh syndrome is one of these rare inherited neurometabolic diseases, with more than 75 causal genes identified in both nuclear and mitochondrial DNA. It has an early onset, affecting most patients within their first year of life, although cases during teenage years and adulthood have been reported (Finsterer, 2008; Lake et al., 2016). As it is a highly heterogenous disease, the establishment of animal and *in vitro* models has been challenging and limited to only select mutations. The few animal models available have been utilized for the development of therapeutic approaches with mixed results. Gene editing using adeno-associated virus in Ndufs4-/- mice has shown partial rescue of the phenotype (Di Meo et al., 2017). Supplementation of nicotinamide riboside to Sco2-/- mice showed improvement of the respiratory chain defect and increased exercise tolerance due to improved mitochondrial biogenesis (Cerutti et al., 2014). Hypoxia and low oxygen availability in the brain have also been shown to increase the life span and improve neurological findings in Ndufs4-/- mice (Ferrari et al., 2017; Jain et al., 2016, 2019).

Molecular testing and prenatal diagnosis of respiratory chain disorders using skin fibroblasts and muscle biopsies for diagnostic and research purposes are becoming mainstream procedures (Baertling et al., 2014; Calvo et al., 2006, 2012; Schubert and Vilarinho, 2020). Nevertheless,

379 heteroplasmy in mitochondrial DNA among tissues can cause less pronounced or absent
380 phenotypes in cultured cells (Baertling et al., 2014). Here we report the characterization and the
381 subsequent generation of brain organoids from three commercially available Leigh syndrome
382 fibroblast cell lines and an age matched control.

383 Three dimensional differentiation generates higher numbers of NPCs and more mature
384 neurons than two dimensional differentiation (Chandrasekaran et al., 2017; Di Lullo and
385 Kriegstein, 2017; Muratore et al., 2014; Paşca et al., 2015) in part due to an improved spatial
386 cellular environment that influences cell fate specification. Tissue architecture, mechanical cues,
387 cell-to-cell communication (Pampaloni et al., 2007), nutrient accessibility, oxygen tension, as well
388 as morphogen gradients characteristic of 3D systems (Tibbitt and Anseth, 2012) aid to
389 recapitulate the development of the central nervous system (CNS) up to approximately 16 weeks
390 post-fertilization (Camp et al., 2015; Paşca et al., 2015). We observed that all the LS cerebral
391 organoids failed to thrive at different time points. Although organoid development initially
392 appeared normal in cell lines with nuclear encoded LS mutations, at later time points, the overall
393 diameter decreased, presumably due to failure to generate upper layer neurons. This reduction
394 of late born neurons may be due to the overall reduction in the PAX6+ NPCs in both PDH and
395 DLD compared to controls. Interestingly, PDH cerebral organoids displayed arrested growth very
396 early on, correlating with the microcephaly observed in the source patient.

397 The increase in the glial-specific marker S100β in DLD and MT-ATP6/PDH organoids could
398 also correlate with the observation that gliosis is a common clinical finding in LS patients (Baertling
399 et al., 2014, 2016; Schubert and Vilarinho, 2020). The formation of lesions in LS has been
400 described as the result of OXPHOS dysfunction and subsequent ATP depletion. Neuronal
401 dysfunction is suspected to trigger chronic gliosis (Baertling et al., 2016). In patients, the gliosis
402 phenotype can be accompanied by vascular hypertrophy and production of excess ROS, which
403 increases neuronal damage (Lake et al., 2015). However, due to the lack of vascularization in the

organoid model, replicating the vascular abnormalities associated with LS is not feasible in this system.

The profound dysregulation of corticogenesis in the double mutant MT-ATP6/PDH, may suggest that some pregnancies harboring LS-causing mutations may not be viable, which could lead to an underestimation of the prevalence of the disease in the population (Feeney et al., 2019). Prenatal genetic evaluation is now being performed for cases where there is a known risk for mitochondrial mutations (Craven et al., 2017; White et al., 1999). This testing can be performed as early as 10-12 weeks post conception and is usually requested if there is a history of a previously affected child or first degree relative (Nesbitt et al., 2014). Interpretation of these tests is challenging in the case of mitochondrial mutations due to heteroplasmy; the biopsied tissues may exhibit a different mutational burden compared with other fetal tissues (Ferlin et al., 1997; Harding et al., 1992; Nesbitt et al., 2014; Steffann et al., 2007).

In a previous study (Hattori et al., 2016), the metabolic signature analysis of iPSCs derived from a mitochondrial encoded LS mutation (m.10191T>C) showed differences in the abundance of pyruvate and lactate, among others. Interestingly, the metabolic difference between control and LS cells was reported to revert back to normal after EB differentiation (Hattori et al., 2016). In our study, metabolomic analysis from neuralized EBs and organoids show that the observed changes in the metabolites are in line with the clinical observations of LS patients. Changes in blood and cerebral spinal fluid concentration of lactate and pyruvate are common diagnostic tools for LS (Hattori et al., 2016) and other mitochondrial diseases (Barshop, 2004; Buzkova et al., 2018; Esterhuizen et al., 2017; Rahman and Rahman, 2018). We also identified trends toward changes in other metabolites, like dihydroorotate and aspartate, that highlight the overall impact of LS mutations at different steps of the metabolic pathway (ETC complex III, TCA cycle and *de novo* nucleotide synthesis, and NADH/NAD+ ratio).

The metabolic dysregulation of the affected tissues in LS may have a direct effect on mitochondrial morphology and function. Mitochondrial fragmentation is a hallmark of glycolytic cell types such

as stem cells and cancer cells (Chen and Chan, 2017; Rastogi et al., 2019). Moreover, neurogenesis defects have been observed in the context of mitochondrial morphology dysregulation and are considered to be upstream regulators of self-renewal and cell fate decisions in stem cells (Khacho et al., 2016). In addition, energetic requirements have been shown to directly impact the capacity of progenitor cells to migrate and thrive in 3D environments (Zanotelli et al., 2018, 2019). Hence, mitochondrial morphology disruption observed in the double mutant MT-ATP6/PDH organoids is expected when analyzed in conjunction with the metabolic and developmental profile of these mutant organoids. To our knowledge, this is the first time that mitochondrial morphology in the cortex has been analyzed in a human model system of LS brain development and highlights the potential importance of mitochondria network plasticity for the proper specification of cell fate and survival.

Here, we presented the characterization of three commercially available LS cell lines from fibroblasts to cerebral organoids. We were able to identify new genetic alterations in these samples by using whole exome sequencing and mitochondrial DNA sequencing. We described the effects of these mutations in a 3D cerebral organoid system. We aim to provide a comprehensive phenotypic characterization of available patient samples to encourage their utilization as model systems for uncovering the mechanisms underlying neuronal cell death in the context of LS and for drug discovery.

Figure Legends

Figure 1. Whole exome sequencing identifies novel mutations in Leigh syndrome fibroblasts. A. Schematic of the WES and mitochondrial sequencing workflow. B. Representation of whole genome sequencing data, highlighting the top 20 genes containing high impact indels. C. Representation of whole genome sequencing data, highlighting the top 20 genes containing high impact SNPs (increased likelihood of disrupting protein function). D. Mitochondrial sequencing identifies novel mutations in LS fibroblasts. Representation of mitochondrial sequencing data, highlighting mitochondrial genes containing mutations (transitions, deletions, or transversions). Red dots: represent DLD line. Green dots: represent the PDH line. Orange dots: represent the MT-ATP6/PDH line.

Figure 2. Induced pluripotent stem cells derived from Leigh syndrome patient fibroblasts are capable of differentiation into specific lineages. A-B. Representative images of the ectoderm marker Pax6 (A) and qPCR for the ectodermal genes *GATA3* and *PAX6* (B). C-D. Representative images of the endoderm marker SOX17 (C) and qPCR for the ectodermal genes *CDX2* and *SOX17* (D). E-F. Representative images of the mesoderm markers Brachyury and CXCR4 (E) and qPCR for the mesodermal genes *TBXT* and *NCAM* (F). Scale bar: 100μm.

Figure 3. Leigh syndrome derived NPCs are multipotent and do not show aberrant mitochondrial morphology compared to control. A. Schematic of two-dimensional neural differentiation. B. Immunoblot of protein expression of neural markers Pax6, Nestin, and Sox2. Scale bar: 100μm C. Immunofluorescence for multipotency markers. Neural progenitor cells stained by Pax6 and Nestin, neurons marked with βIII-tubulin, oligodendrocytes stained with Olig2 and astrocytes are marked with S100β. D. Representative super-resolution images of mitochondrial morphology (Mitotracker) in LS and control NPCs. Scale bar: 5μm.

476 **Figure 4.** Generation of neuralized EBs from Leigh syndrome derived iPSCs lead to changes in
477 EB diameter and the abundance of metabolites involved in central carbon metabolism. A.
478 Schematic of EB generation protocol. B. Embryoid body diameter is increased in the three LS cell
479 lines. C. Metabolite abundance pathway analysis. Top metabolic pathways affected in day 10 LS
480 neuralized EBs. Statistical p values from enrichment analysis are adjusted for multiple testing.
481 Total: number of total compounds in the pathway. Hits: matched number from the uploaded data.
482 Raw p: original p value calculated from the enrichment analysis. Holm p: p value adjusted by
483 Holm-Bonferroni method. FDR p: adjusted p value using False Discovery Rate. Impact: pathway
484 impact value calculated from pathway topology analysis. *p < 0.05; **p < 0.001, ***p < 0.0001.
485
486 **Figure 5.** Three-dimensional differentiation reveals abnormalities during induction of neural
487 rosettes in LS cell lines. A. Schematic of neural rosette generation protocol. B-D. Representative
488 confocal images of neural rosettes (C) show decreased numbers of neural rosettes per field in
489 the DLD mutant line (D). Quantification of the lumen area (μm^2) indicate increased lumen area in
490 the PDH and MT-ATP6/PDH mutant cell lines and a decreased lumen area in the DLD mutant
491 line. Scale bar: 50μm. *p < 0.05; **p < 0.001, ***p < 0.0001.
492
493 **Figure 6.** Leigh syndrome derived brain organoids show a reduction in size and MT-ATP6/PDH
494 mutant brain organoids show defects in SVZ/VZ and CP formation and aberrant mitochondrial
495 morphology in Sox2+ cells. A. Schematic of brain organoid generation protocol. B. Brain organoid
496 growth curves. LS derived brain organoids show reduction in size when grown for 100 days. C.
497 Schematic representation of the expected organization of the brain organoids at day 30. D-E.
498 Representative immunostaining confocal images of day 30 brain organoids. MT-ATP6/PDH
499 mutant present a severe disorganization of the SVZ/VZ markers Pax6 and Tbr2, as well as the
500 neural progenitor marker Nestin (D). MT-ATP6/PDH mutant do not express the CP and deep layer
501 markers CTIP2 and TBR1 (E). Scale bar: 100μm. F. Representative confocal images of day 30

brain organoids showing mitochondrial morphology (Tomm20). The red line divides the Sox2+ neural progenitor cells surrounding the lumen (L) from newly committed neurons. MT-ATP6/PDH mutant organoids show disorganization and fragmentation of the mitochondrial network compared to control. Scale bar: 10μm. SVZ: subventricular zone, VZ: ventricular zone, CP: cortical plate, MZ: marginal zone. * $p < 0.05$ for Control and PDH mutant; ǂ $p < 0.05$ for Control and DLD mutant, ф $p <$ for Control and MT-ATP6/PDH mutant.

Figure 7. Leigh syndrome derived brain organoids show defects in cortical layer formation at day 100. A. Schematic representation of the expected organization of the brain organoids at day 100. B-D. Representative immunostaining confocal images of day 100 brain organoids. LS derived brain organoids present reduced expression of the upper layer markers SATB2 (B), BRN2 (C) and CUX1 (D) and deep layer marker CTIP2 (C & D). Increased expression of the astrocyte marker S100β was also noticed in the MT-ATP6/PDH mutant line. Scale bar: 100μm. SVZ: subventricular zone, VZ: ventricular zone, DL: deep layers UL: upper layers, MZ: marginal zone.

STAR Methods

Key Resource Table

REAGENT or RESOURCE	SOURCE	IDENTIFIER
ANTIBODIES		
Primary Antibodies (Immunocytochemistry)		
Rabbit anti-PAX6	Cell Signaling Technology	Cat # 60433, AB_2797599
Rabbit anti-SOX17	Cell Signaling Technology	Cat # 81778S, AB_2650582
Rabbit anti-BRACHYURY	Cell Signaling Technology	Cat # 81694S, AB_2799983
Mouse anti-CD184 (CXCR4)	STEMCELL Technologies	Cat # 60089
Mouse anti-β3 tubulin	Cell Signaling Technology	Cat # 4466, AB_10270973
Rabbit anti-S100	Abcam	Cat # ab868, AB_306716
Mouse anti-Olig2	Millipore Sigma	Cat # MABN50, AB_10807410
Rat anti-α tubulin	Thermo Fisher Scientific	Cat # MA180017, AB_2210201
Mouse anti-ZO-1	Thermo Fisher Scientific	Cat # 339100, AB_2533147
Rabbit anti-CDK5RAP2	Bethyl Laboratories	Cat # IHC00063, AB_2076863
Mouse anti-Nestin	STEMCELL Technologies	Cat # 60091, AB_2650581
Chicken anti-TBR2	Millipore Sigma	Cat # AB15894, AB_10615604
Mouse anti-Reelin	Millipore Sigma	Cat # MAB5366, AB_2285132
Rat anti-CTIP2	Abcam	Cat # ab18465, AB_2064130
Rabbit anti-TBR1	Abcam	Cat # ab31940, AB_2200219
Rabbit anti-TOM20	Cell Signaling Technology	Cat # 42406, AB_2687663
Mouse anti-SATB2	Abcam	Cat # ab51502, AB_882455
Mouse anti-BRN2 (POU3F2)	Millipore Sigma	Cat # MABD51, AB_11204531
Mouse anti-CASP (CUX1)	Abcam	Cat # ab54583, AB_941209
Secondary Antibodies (Immunocytochemistry)		
Goat anti Chicken Alexa Fluor 647	Thermo Fisher Scientific	Cat # A-21449, AB_2535866
Goat anti Rat Alexa Fluor 647	Thermo Fisher Scientific	Cat # A-21247, AB_2535864
Donkey anti Rabbit Alexa Fluor 647	Thermo Fisher Scientific	Cat # A-31573, AB_2536183
Donkey anti Mouse Alexa Fluor 647	Thermo Fisher Scientific	Cat # A-31571, AB_162542
Donkey anti Rabbit Alexa Fluor 546	Thermo Fisher Scientific	Cat # A-10040, AB_2534016

Donkey anti Mouse Alexa Fluor 546	Thermo Fisher Scientific	Cat # A-10036, AB_2534012
Donkey anti Rabbit Alexa Fluor 488	Thermo Fisher Scientific	Cat # A-21206, AB_2535792
Donkey anti Mouse Alexa Fluor 488	Thermo Fisher Scientific	Cat # A-21202, AB_141607
Primary Antibodies (Western Blotting)		
Rabbit anti-PAX6	Cell Signaling Technology	Cat # 60433, AB_2797599
Mouse anti-Nestin	STEMCELL Technologies	Cat # 60091, AB_2650581
Rabbit anti-Sox2	Cell Signaling Technology	Cat # 3579, AB_2195767
Mouse anti- α tubulin	Sigma-Aldrich	Cat # T9026, AB_477593
Secondary Antibodies -HRP conjugated (Western Blotting)		
Peroxidase AffiniPure Donkey Anti-Rabbit IgG (H+L)	Jackson ImmunoResearch Inc	Cat # 711-035-152, AB_10015282
Peroxidase AffiniPure Donkey Anti-Mouse IgG (H+L)	Jackson ImmunoResearch Inc	Cat # 715-035-151, AB_2340771
CHEMICALS, PEPTIDE, AND RECOMBINANT PROTEINS		
Y-27632 Rho/Rock pathway inhibitor	STEMCELL Technologies	Cat # 72307
Dorsomorphin	Millipore Sigma	Cat # P5499
SB431542	REPROCELL	Cat # 04-0010-10
Etoposide	Millipore Sigma	Cat # E1383
Carbonyl cyanide 3-chlorophenylhydrazone (CCCP)	Sigma Aldrich	Cat # C2759
Nocodazole	Sigma Aldrich	Cat # M1404
Neocarzinostatin	Sigma Aldrich	Cat # 9162
CRITICAL COMMERCIAL ASSAYS AND KITS		
PluriTest Assay	Thermo Fisher Scientific	Cat# A38154
KaryoStat Assay	Thermo Fisher Scientific	Cat# A38153
Mitochondrial DNA sequencing	Girihlet	
Whole Exome sequencing	Genewiz LLC	
CytoTune iPS 2.0 Sendai Reprogramming Kit	Thermo Fisher Scientific	Cat # A16517
STEMdiff Trilineage Differentiation Kit	STEMCELL Technologies	Cat# 05230

NeuroCult™ media	STEMCELL Technologies	Cat # 05752
Astrocyte medium	ScienCell	Cat # 1801
CellTiter Blue Viability Assay	Promega	Cat # G8081
DEPOSITED DATA		
Raw and analyzed sequencing data	Done by Creative Solutions (J.P.C, Vanderbilt University	https://www.ncbi.nlm.nih.gov/sra/PRJNA626388 https://vandydata.github.io/Romero-Morales-Gama-Leigh-Syndrome-WES/
EXPERIMENTAL MODELS: CELL LINES		
AG16409 control fibroblasts	Coriell Institute	https://www.coriell.org/0/Sections/Search/Sample_Detail.aspx?Ref=AG16409&Product=CC
GM13411 (MT-ATP6/PDH) fibroblasts	Coriell Institute	https://www.coriell.org/0/Sections/Search/Sample_Detail.aspx?Ref=GM13411&Product=CC
GM03672 (PDH Mutant) fibroblasts	Coriell Institute	https://www.coriell.org/0/Sections/Search/Sample_Detail.aspx?Ref=GM03672&Product=CC
GM01503 (DLD Mutant) fibroblasts	Coriell Institute	https://www.coriell.org/0/Sections/Search/Sample_Detail.aspx?Ref=GM01503&Product=CC
SEQUENCE-BASED REAGENTS		
Primers for Trilineage assay		
OCT4	Integrated DNA Technologies	Forward GGGCTCTCCCATGCATTCAAAC Reverse CACCTTCCCTCCAACCAGTTGC
NANOG	Integrated DNA Technologies	Forward TGGGATTTACAGGCGTGAGCCAC Reverse AAGCAAAGCCTCCCAATCCCAAAC
GAPDH	Integrated DNA Technologies	Harvard PrimerBank, ID: 378404907c2 Forward ACAACTTTGGTATCGTGGAAGG Reverse GCCATCACGCCACAGTTTC
GATA3	Integrated DNA Technologies	Forward TGGAGGAGGAATGCCAATGGG Reverse GCCGGGTTAAACGAGCTGTTCTTG
PAX6	Integrated DNA Technologies	Harvard Primer Bank, ID: 189083679c1 Forward TGGGCAGGTATTACGAGACTG Reverse ACTCCCGCTTATACTGGGCTA
CDX2	Integrated DNA Technologies	Forward CTGGAGCTGGAGAAGGAGTTTCAC Reverse GACACTTCTCAGAGGACCTGGCTG
SOX17	Integrated DNA Technologies	Harvard Primer Bank, ID:145275218c1 Forward GTGGACCGCACGGAATTTG Reverse GGAGATTCACACCGGAGTCA

TBXT	Integrated DNA Technologies	Forward ACAATGCCAGCCCACCTACCAG Reverse CGTACTGGCTGTCCACGATGTCTG
NCAM	Integrated DNA Technologies	Harvard Primer Bank, ID:316659209c1 Forward GGGGTTGCTTGTCAGTAGC Reverse TTCAGGTTCACCAATCGCTGT
SOFTWARE AND ALGORITHMS		
Image Studio™ Lite	LI-COR	https://www.licor.com/bio/image-studio-lite/download
Fiji	Schindelin et al., 2012	https://imagej.net/Fiji
GraphPad Prism v8.1.2	GraphPad	https://www.graphpad.com/scientific-software/prism/
NIS-Elements	Nikon Instruments	https://www.microscope.healthcare.nikon.com/products/software/nis-elements
MetaboAnalyst 4.0	(Chong and Xia, 2018; Chong et al., 2018, 2019; Xia and Wishart, 2010, 2011a, 2011b; Xia et al., 2009)	https://www.metaboanalyst.ca/home.xhtml
SnpSift	(Cingolani et al., 2012)	http://snpeff.sourceforge.net/SnpSift.html
R 3.5.3	R Foundation	https://www.r-project.org/
BioCircos	(Cui et al., 2016)	https://cran.r-project.org/web/packages/BioCircos/index.html
OTHER		
Mitotracker Red CMXRos	Fisher Scientific	Cat # M7512
Matrigel™	Corning	Cat # 354277
Gentle dissociation solution	STEMCELL Technologies	Cat # 07174
Aggrewell™ 800 24-well plate	STEMCELL Technologies	Cat # 34815
AggreWell™ Rinsing Solution	STEMCELL Technologies	Cat # 07010
STEMdiff™ Cerebral Organoid Kit	STEMCELL Technologies	Cat # 08570
STEMdiff™ Cerebral Organoid Maturation Kit	STEMCELL Technologies	Cat # 08571

Lead Contact and Materials Availability

Further information and requests for resources and reagents should be directed to the Lead Contact, Vivian Gama (vivian.gama@vanderbilt.edu).

Experimental Model and Subject Details

The Coriell cell line IDs were as follows: GM01503, GM03672, GM1341. Information about the Leigh syndrome cell lines used in this study can be found in Supplementary Table1. Control skin fibroblast cell line AG16409 was also obtained from Coriell Institute, Philadelphia, PA. The donor was a 12-year-old apparently healthy Caucasian male.

Fibroblasts were maintained in Dulbecco's Modified Eagle Medium: Nutrient Mixture F-12 DMEM/F-12 (Gibco cat # 11330032) supplemented with 10% Fetal bovine serum (Sigma cat# F2442) in 100mm cell culture plates (Eppendorf, cat # 0030702115) in a 37°C 5% CO2 incubator.

Method Details

Whole Exome sequencing

Fibroblast cell pellets from each cell line (>1 million cells) were shipped on dry ice for whole genome exome sequencing to Genewiz, Plainfield, NJ. The Illumina HiSeq-X was used to perform 150nt paired-end sequencing.

Mitochondrial sequencing

Fibroblast cell pellets from each patient (>1 million cells) were shipped on dry ice for mitochondrial sequencing to Girihlet Inc. Oakland, CA. The sequencing configuration used was 80bp single-end sequencing, 20 million reads per sample.

hiPSC Generation and Characterization

Human fibroblasts were purchased from healthy control and patients (Coriell Institute, Philadelphia, PA, USA). Induced pluripotent stem cells were derived from human fibroblasts using Sendai virus-based reprogramming kit (CytoTune-iPS Sendai Reprogramming Kit; cat #. A13780-01; Thermo Fisher), according to manufacturer's instructions. After 3-4 weeks, 2-3 colonies per sample were transferred to fresh 6-well plates and were expanded and gardened for 3 passages

before freezing. All iPSC cell lines were maintained in E8 medium in plates coated with Matrigel (Corning, cat # 354277) at 37°C with 5% CO_2. Culture medium was changed daily. Cells were checked daily for differentiation and were passaged every 3-4 days using Gentle dissociation solution (STEMCELL Technologies, cat # 07174). All experiments were performed under the supervision of the Vanderbilt Institutional Human Pluripotent Cell Research Oversight (VIHPCRO) Committee.

Analysis of Pluripotency

Pluripotency of each iPSC clone was determined using a microarray-based tool known as PluriTest (Thermo Fisher; cat# A38154) as an alternative to the teratoma assay. Samples were outsourced to Thermo Fisher for PluriTest and further analysis. Low passage iPSC cell pellets (>1 million cells) were frozen and shipped on dry ice. Additionally, expression of pluripotency genes POU5F1 and NANOG was assessed by qPCR.

Analysis of Chromosomal abnormalities

The presence of any chromosomal abnormalities in the newly generated iPSCs was determined using a microarray-based tool known as KaryoStat (Thermo Fisher; cat# A38153) as an alternative to chromosomal G-banding. Samples were outsourced to Thermo Fisher for KaryoStat and further analysis. Low passage iPSC cell pellets (>1 million cells) were frozen and shipped on dry ice to Thermo Fisher.

Trilineage differentiation

The STEMdiff Trilineage differentiation kit (STEMCELL Technologies, cat# 05230) was used to functionally validate the ability of newly established iPSCs to differentiate into three germ layers, as per the manufacturer's instructions. Single cell suspensions of 2x106 cells/well, $5x10^5$ cells/well, $2x10^6$ cells/well were seeded for ectoderm, mesoderm and endoderm, respectively, in

their corresponding medium at day 0 in 6 well plates. The cultures were maintained for 7 days, 5 days, and 5 days for ectoderm, mesoderm, and endoderm, respectively. The differentiation was assessed by immunocytochemistry and qPCR.

NPC differentiation and multipotency characterization

For monolayer differentiation of the iPSCs into NPCs, cells were dissociated into single cells using Gentle Cell Dissociation Reagent (STEMCELL Technologies, cat # 07174) for 8 minutes at 37°C. Live cell counts were performed using Trypan blue (0.4%) staining (Invitrogen, cat # T10282) using a Countess™ Automated Cell Counter. Cell were then seeded in a Matrigel coated 6-well plate (Eppendorf, cat # 0030720113) to a $2.5x10^6$ cells/well with dual SMAD inhibitor media supplemented with Dorsomorphin (1µM) and SB431542 (10µM) (Chambers et al., 2009) supplemented with ROCK inhibitor. Daily media changes were performed and passaging of the cells was done every 7-9 days. Cells for NPC marker analysis were collected at the end of the first 9 days of differentiation.

Mitochondrial imaging was performed by adding 100nM MitoTracker Red CMXRos (Thermo Fisher Scientific #M7512) to the media for 20 minutes before PFA fixation. Super-resolution images were acquired using a Nikon SIM microscope equipped with a 1.49 NA 100x Oil objective an Andor DU-897 EMCCD camera.

For multipotency analysis, culture media was changed to NeuroCult™ media and maintained for 4 weeks. Samples were then fixed and stained for neuron and oligodendrocyte markers. Astrocyte differentiation was performed by seeding on a Matrigel coated plate $1.5x10^6$ cells/cm^2 (TCW et al., 2017). The following day, media was changed to Astrocyte medium (ScienCell, cat # 1801) and maintained for 20 days. Full media changes were done every 2 days. Samples were then fixed and stained for an astrocyte marker. Images were acquired with a Nikon Ti Eclipse microscope equipped with a Nikon DS-Qi2 camera and 0.75 NA 20X air objective.

603 **Neural rosette differentiation**

604 To generate neural rosettes, we dissociated the cells into single cell suspension and seeded
605 $3.0x10^6$ cells/well of an Aggrewell™ 800 in dual SMAD inhibitor media. EBs were incubated at
606 37°C with 5% CO2, with minimal disruption during the first 48 hours. Media changes, 50-75% of
607 the total volume, were performed every 2 days. On Day 5, EBs were harvested according to the
608 manufacturer protocol and transferred to a 35mm imaging plate (Cellvis, cat # D35-14-1.5-N)
609 coated with Matrigel. Daily media changes were performed up to day 9 when cells were fixed with
610 100% ice-cold Methanol (Fisher Scientific, cat # A454-4). Images were acquired with an Andor
611 DU-897 EMCCD camera mounted on a Nikon Spinning Disk Microscope equipped with a 0.45
612 NA 10X and 0.75 NA 20X objectives. Data analysis was performed using NIS Elements. A *Neural*
613 *Rosette Quantification* macro was developed to measure the rosette lumen area based on the
614 ZO-1 staining channel. Max IPs were generated per ROI, followed by advanced denoise of the
615 image. Binary mask intensity thresholding for the ZO-1 was done using control images. Measured
616 data was exported to an Excel file.

617

618 **Cerebral Organoids**

619 Cerebral organoids were generated as described in (Romero-Morales et al., 2019) with some
620 modifications. Briefly, organoids were generated using the STEMdiff™ Cerebral Organoid Kit
621 (STEMCELL Technologies; Cat# 08571, 08570). iPSCs were dissociated into single cells using
622 Gentle Cell Dissociation Reagent (STEMCELL Technologies, cat # 07174) for 8 minutes at 37°C.
623 Homogeneous and reproducible EBs were generated by using 24-well plate AggreWell™ 800
624 (STEMCELL Technologies, cat # 34815). On Day 7, high quality EBs were embedded in Matrigel
625 (Corning, cat # 354277). On Day 10, the Matrigel coat was broken by vigorously pipetting up and
626 down and the healthy organoids were transferred to a 60mm low attachment culture plate
627 (Eppendorf, cat # 003070119). The plates were then moved to a 37°C incubator and to a Celltron
628 benchtop shaker for CO2 incubators (Infors USA, cat # I69222) set at 85rpm. Full media changes

were performed every 3–4 days. Transmitted-light images were acquired using an EVOS® XL Core Imaging System. The software used for processing was ImageJ.

Organoid tissue preparation and Immunohistochemistry

Tissue preparation was performed as described in (Romero-Morales et al., 2019). Briefly, organoids were fixed in 4% Paraformaldehyde in Phosphate Buffered Saline (PBS), washed 3 times with PBS and then incubated in 30% sucrose solution overnight at 4°C. Organoids were embedded in 7.5% gelatin/10% sucrose solution (Sigma, catalog G1890-100G and S7903-250G) and sectioned with a cryostat (Leica CM1950) at 15um thickness. For immunostaining, slides were washed with PBS before permeabilization with 0.2% Triton-X in PBS for 1 hr. Tissues were blocked with blocking medium consisting of 10% donkey serum in PBS with 0.1% Tween-20 (PBST) for 30 min. Incubation with primary and secondary antibodies was done using standard methods. Confocal images of the organoids were acquired using an Andor DU-897 EMCCD camera mounted on a Nikon Spinning Disk Microscope0.45 NA 10X and 0.75 NA 20X air objectives (macro structures) and 1.49 NA 100x oil objective (mitochondria imaging). The software used for image acquisition and reconstruction was NIS-Elements Viewer (Nikon).

RNA Extraction and Synthesis of cDNA

Cells cultured in 6 well plate, were collected after a wash with PBS, using 600µl Trizol reagent. The samples were spun down at 12,000 g after addition 130 µl of chloroform and incubated at room temperature for 3 minutes. The aqueous phase of the sample was collected 200µl at a time until reaching the edge of phase separation. RNA precipitation was done by incubating with 300µl of isopropanol for 25 minutes, followed by centrifugation at 12,000 g for 10 min at 4°C. RNA pellet was washed with ethanol, semidried, and resuspended in 30µl of DEPC water. After quantification and adjusting volume of all the sample to 1µg/µl, the samples were treated with DNAse (New

England Biolabs, cat # M0303). 10µl of this volume was used to generate cDNA using manufacturer's protocol (Thermofisher, cat#4368814)

Quantitative RT PCR

1ug of cDNA sample was used to run a q-PCR for the primers mentioned in the table. QuantStudio 3 Real-Time PCR machine, SYBR green master mix (Thermo Fisher, cat#4364346) and manufacturer instructions were used to set up the assay.

Immunocytochemistry

Cells were fixed with 4% paraformaldehyde (Electron Microscopy Sciences, cat # 15710-S) in PBS for 20 min at 4ºC. Blocking and permeabilization were done in 5% Donkey serum (Jackson ImmunoResearch Inc, cat # 017-000-121) + 0.3% Triton X-100 (Sigma Aldrich, cat # T9284) in TBS for 1 hr at room temperature. After this, cells were treated with primary and secondary antibodies using standard methods. Cells were mounted in Vectashield (Vector Laboratories, cat # H-1000) prior to imaging.

Western Blotting

Cultured cells were lysed in 1% Triton buffer containing PMSF (ThermoFisher Scientific, cat # 36978), PhosSTOP (Roche, cat # 4906837001), and protease inhibitor cocktail (Roche, cat # 4693132001). Protein concentrations were determined using the bicinchoninic acid (BCA) method (Thermo Scientific, cat # 23227). Gel samples were prepared by mixing 30µg of protein with LDS sample buffer (Life Technologies, cat # NP0007) and 2-Mercaptoethanol (BioRad, cat # 1610710) and boiled at 95°C for 5 minutes. Samples were run on 4-20% Mini-PROTEAN TGX precast gels (BioRad, cat # 4561096) and transferred onto polyvinylidene difluoride (PVDF) membrane (BioRad, cat # 1620177) overnight at 4°C. Membranes were blocked in 5% milk in TBST prior to

679 primary antibody incubation. Antibodies used for Western blotting are described in Key Resource
680 table.
681
682 **Cell titer blue assay**
683 After the 24-h exposure to individual treatments of 50μM etoposide, 80μM CCCP, 100ng/mL
684 nocodazole, and 5ng/mL neocarzinostatin, 20 μl of Cell Titer Blue reagent from Cell Titer Blue
685 assay (Promega, cat # G8081) was added to each well of 96 well plate. Background fluorescence
686 was calculated by adding 10% Triton in PBS to some wells. The fluorescence generated by the
687 reduction of resazurin to resorufin by live cells was measured using a Beckman coulter DTX 880
688 multimode plate reader (Beckman Coulter, Brea, California) (570/600 nm).
689
690 **Metabolomics analysis**
691 Neuralized embryoid bodies were generated by seeding $3x10^6$ cells/well in an Aggewell800^{TM}.
692 Media change was performed at day 2 and 4. On day 5, EBs were transferred to a low attachment
693 60mm plate and maintained in suspension with daily media changes. On day 10, ~150 EBs were
694 collected in a 1.5mL centrifuge tube, rinsed with ice-cold sterile 0.9% NaCl and flash-frozen in
695 liquid nitrogen. For organoids, at least 4 individual organoids were collected at day 40, rinsed with
696 ice-cold sterile 0.9% NaCl and flash-freeze in liquid nitrogen.
697 For metabolite extraction, cells were resuspended in 225uL of cold 80% HPLC grade
698 methanol/20% HPLC grade water per $1x10^6$ cells. After resuspension, cells were flash frozen in
699 liquid nitrogen and thawed rapidly in 37°C water bath 3 times. Next debris were removed by
700 centrifugation at max speed in a tabletop microcentrifuge at 4°C for 15 min. Metabolite-containing
701 supernatant was transfer to a new tube, dried, and resuspended in 50% acetonitrile while the
702 pellet was used for protein quantification. Samples were analyzed by Ultra-High-Performance
703 Liquid Chromatography and High-Resolution Mass Spectrometry and Tandem Mass
704 Spectrometry (UHPLC-MS/MS). Specifically, the system consisted of a Thermo Q-Exactive in line

with an electrospray source and an Ultimate3000 (Thermo) series HPLC consisting of a binary pump, degasser, and auto-sampler outfitted with an Xbridge Amide column (Waters; dimensions of 4.6mm × 100mm and a 3.5µm particle size). Mobile phase A contained 95% (vol/vol) water, 5% (vol/vol) acetonitrile, 10mM ammonium hydroxide, 10mM ammonium acetate, pH = 9.0; and mobile phase B was 100% Acetonitrile. The gradient was as follows: 0 min, 15% A; 2.5 min, 30% A; 7 min, 43% A; 16 min, 62% A; 16.1-18 min, 75% A; 18-25 min, 15% A with a flow rate of 400µL/min. The capillary of the ESI source was set to 275°C, with sheath gas at 45 arbitrary units, auxiliary gas at 5 arbitrary units, and the spray voltage at 4.0kV. In positive/negative polarity switching mode, an m/z scan range from 70 to 850 was chosen and MS1 data was collected at a resolution of 70,000. The automatic gain control (AGC) target was set at $1x10^6$ and the maximum injection time was 200 ms. The top 5 precursor ions were subsequently fragmented, in a data-dependent manner, using the higher energy collisional dissociation (HCD) cell set to 30% normalized collision energy in MS2 at a resolution power of 17,500. Data acquisition and analysis were carried out by Xcalibur 4.1 software and Tracefinder 4.1 software, respectively (both from Thermo Fisher Scientific). The peak area for each detected metabolite was normalized by the total ion current which was determined by integration of all of the recorded peaks within the acquisition window.

Bioinformatic Analysis

Bioinformatic analysis began with Variant Call Format (VCF) files provided by GENEWIZ (see *Whole Exome sequencing* section above), both for SNP and indels. SnpSift version 4.3t (PMID: 22435069) was used to process and filter these files for downstream analysis. Details extracted included gene symbol, Entrez gene ID and name, UniProt ID, Ensembl ID, chromosome and position, reference variant, alternative variant, quality of the call, allele name, type of SNP, impact of the SNP, and the genotype of each sample. From these filtered outputs, we generated

SNP/indel reports that allowed us to look at sample-specific SNPs and indels, as well as perform aggregate-level functions for grouping and statistical analysis.

To generate the SNP/indel circular chromosome plots, the top 20 genes that had variants in all three samples were plotted, ranked by frequency of variants per gene. The outside track is used to visualize the chromosomes and marked gene locations. For each sample, we used a single track to show the variant frequency as a circular scatter plot, with the height of the scatter points representative of the variant quality metric, which is a Phred-scaled probability that a REF/ALT polymorphism exists at the variant site. Similarly, for SNPs in the mitochondrial chromosome, we used the same approach for visualization.

Quantification and Statistical Analysis

No statistical methods were used to pre-determine sample sizes. All experiments were performed with a minimum of 3 biological replicates, unless specified. Statistical significance was determined by unpaired Student's t-test or by one- or two-way ANOVA as appropriate for each experiment. GraphPad Prism v8.1.2 was used for all statistical analysis and data visualization.

Error bars in all bar graphs represent standard error of the mean or standard deviation as described for each Figure, while scattered dot plots were represented with boxes (with median and SD) and whiskers (minimum and maximum values).

For neural rosette experiments, ROI were randomly selected using the nuclear (DAPI) staining channel. Images were processed with NIS Elements software with our Neural rosette lumen identification Macro. Outliers were removed from the neural rosette area analysis as post-processing quality control for the NIS Element macro using GraphPad Prism v8.1.2. ROUT (Robust regression and Outlier removal) method was used with a False Discovery Rate of 1%.

For cerebral organoid experiments, 4 independent batches were generated. At timepoints day 30 and day100, at least 5 organoids per cell line were collected. Immunofluorescence images of at least 3 independent organoids were acquired per condition slide. Image processing was done by

NIS Elements and Fiji software. Organoid efficiency evaluation was performed at day 10 using 4X transmitted-light images acquired using an EVOS® XL microscope. Two observers were blinded to the cell line identifier and counted the number of normal and defective (no epithelial buds or more than 75% of the area is not developed) organoids. Criteria for normal and defective organoids was based on (Lancaster and Knoblich, 2014).

For the metabolomics experiments, two independent LC/MS runs of ~150-200 neuralized EBs/cell line/replica were utilized with enough material to account for $3x10^6$ cells/run. For the cerebral organoid metabolomics, one replica of day 40 organoids was performed, with 4 samples per genotype.

Software and Data Availability

All raw data in FastQ format for whole exome sequencing and mitochondrial sequencing have been deposited to the Short Read Archive as BioProject PRJNA626388, available at https://www.ncbi.nlm.nih.gov/sra/PRJNA626388. All source code and document are available via https://vandydata.github.io/Romero-Morales-Gama-Leigh-Syndrome-WES/.

Author contributions

A.R.M. and V.G. designed experiments, interpret the data and wrote the manuscript. A.R.M., A.R., and M.L.R. performed experiments and analyzed data with technical support of H.T. J.P.C. and L.H. analyzed the genomic data, generated the corresponding figures and the associated method section. P.M.A provided the pluripotency data analysis and technical support for data analysis. B.M generated the neural rosette analysis macro for NIS Elements. N.S.C. and G.S.M provided technical support, led experimental design and data analysis for metabolomics and its corresponding method section.

Conflict of interests

782 The authors declare no competing interests.

783

784 **Acknowledgements**

785 We thank Dr. Nicholas Mignemi (Vanderbilt Nikon Center for Excellence) for his technical support
786 with image acquisition and processing. We would like to thank members of the Gama Laboratory
787 for helpful discussions and comments to the manuscript. Funding was provided by the following
788 grants: 1R35GM128915-01 (to VG); 1R21 CA227483-01A1 (to VG); the Precision Medicine and
789 Mental Health Initiative sponsored by the Vanderbilt Brain Institute (to VG). Image acquisition and
790 analysis were performed in part through the use of the Nikon Center of Excellence within the
791 Vanderbilt Cell Imaging Shared Resource (supported by NIH grants CA68485, DK20593,
792 DK58404, DK59637 and EY08126), Vanderbilt University Medical Center's Translational
793 Pathology Shared Resource supported by NCI/NIH Cancer Center Support Grant 2P30
794 CA068485-14, and the Vanderbilt Mouse Metabolic Phenotyping Center Grant 5U24DK059637-
795 13. Whole exome sequencing and mitochondrial sequencing results were analyzed by Creative
796 Solutions. Metabolite measurements were performed by the Northwestern University RHLCCC
797 Metabolomics Core (Peng Gao) and were supported by the following NIH grants to N.S.C.:
798 NIH2PO1HL071643-11A1, NIH1R35CA197532-01, NIH1PO1AG049665-01 and NIH/NCI grant
799 to G.S.M: T32CA09560.

800

References

Agana, M., Frueh, J., Kamboj, M., Patel, D.R., and Kanungo, S. (2018). Common metabolic disorder (inborn errors of metabolism) concerns in primary care practice. Ann. Transl. Med. *6*, 469–469.

Albright, C.D., Friedrich, C.B., Brown, E.C., Mar, M.H., and Zeisel, S.H. (1999a). Maternal dietary choline availability alters mitosis, apoptosis and the localization of TOAD-64 protein in the developing fetal rat septum. Dev. Brain Res. *115*, 123–129.

Albright, C.D., Tsai, A.Y., Friedrich, C.B., Mar, M.-H., and Zeisel, S.H. (1999b). Choline availability alters embryonic development of the hippocampus and septum in the rat. Dev. Brain Res. *113*, 13–20.

Angelova, M.T., Dimitrova, D.G., Dinges, N., Lence, T., Worpenberg, L., Carré, C., and Roignant, J.Y. (2018). The emerging field of epitranscriptomics in neurodevelopmental and neuronal disorders. Front. Bioeng. Biotechnol. *6*, 46.

Baertling, F., Rodenburg, R.J., Schaper, J., Smeitink, J.A., Koopman, W.J.H., Mayatepek, E., Morava, E., and Distelmaier, F. (2014). A guide to diagnosis and treatment of Leigh syndrome. J. Neurol. Neurosurg. Psychiatry *85*, 257–265.

Baertling, F., Klee, D., Haack, T.B., Prokisch, H., Meitinger, T., Mayatepek, E., Schaper, J., and Distelmaier, F. (2016). The many faces of paediatric mitochondrial disease on neuroimaging. Child's Nerv. Syst. *32*, 2077–2083.

Barshop, B.A. (2004). Metabolomic approaches to mitochondrial disease: Correlation of urine organic acids. Mitochondrion *4*, 521–527.

Bridi, R., Latini, A., Braum, C.A., Zorzi, G.K., Wajner, M., Lissi, E., and Dutra-Filho, C.S. (2005). Evaluation of the mechanisms involved in leucine-induced oxidative damage in cerebral cortex of young rats. Free Radic. Res. *39*, 71–79.

Buzkova, J., Nikkanen, J., Ahola, S., Hakonen, A.H., Sevastianova, K., Hovinen, T., Yki-Järvinen, H., Pietiläinen, K.H., Lönnqvist, T., Velagapudi, V., et al. (2018). Metabolomes of mitochondrial diseases and inclusion body myositis patients: treatment targets and biomarkers. EMBO Mol. Med. *10*.

Calvo, S., Jain, M., Xie, X., Sheth, S.A., Chang, B., Goldberger, O.A., Spinazzola, A., Zeviani, M., Carr, S.A., and Mootha, V.K. (2006). Systematic identification of human mitochondrial disease genes through integrative genomics. Nat. Genet. *38*, 576–582.

Calvo, S.E., Compton, A.G., Hershman, S.G., Lim, S.C., Lieber, D.S., Tucker, E.J., Laskowski, A., Garone, C., Liu, S., Jaffe, D.B., et al. (2012). Molecular diagnosis of infantile mitochondrial disease with targeted next-generation sequencing. Sci. Transl. Med. *4*, 118ra10-118ra10.

Camp, J.G., Badsha, F., Florio, M., Kanton, S., Gerber, T., Wilsch-Bräuninger, M., Lewitus, E., Sykes, A., Hevers, W., Lancaster, M., et al. (2015). Human cerebral organoids recapitulate gene expression programs of fetal neocortex development. Proc. Natl. Acad. Sci. *112*, 201520760.

Cansev, M. (2006). Uridine and cytidine in the brain: Their transport and utilization. Brain Res. Rev. *52*, 389–397.

Cerutti, R., Pirinen, E., Lamperti, C., Marchet, S., Sauve, A.A., Li, W., Leoni, V., Schon, E.A., Dantzer, F., Auwerx, J., et al. (2014). NAD+-dependent activation of Sirt1 corrects the phenotype in a mouse model of mitochondrial disease. Cell Metab. *19*, 1042–1049.

Chambers, S.M., Fasano, C.A., Papapetrou, E.P., Tomishima, M., Sadelain, M., and Studer, L. (2009). Highly efficient neural conversion of human ES and iPS cells by dual inhibition of SMAD signaling. Nat. Biotechnol. *27*, 275–280.

Chandrasekaran, A., Avci, H.X., Ochalek, A., Rösingh, L.N., Molnár, K., László, L., Bellák, T., Téglási, A., Pesti, K., Mike, A., et al. (2017). Comparison of 2D and 3D neural induction

methods for the generation of neural progenitor cells from human induced pluripotent stem cells. Stem Cell Res. *25*, 139–151.

Chen, H., and Chan, D.C. (2017). Mitochondrial Dynamics in Regulating the Unique Phenotypes of Cancer and Stem Cells. Cell Metab. *26*, 39–48.

Chong, J., and Xia, J. (2018). MetaboAnalystR: an R package for flexible and reproducible analysis of metabolomics data. Bioinformatics *34*, 4313–4314.

Chong, J., Soufan, O., Li, C., Caraus, I., Li, S., Bourque, G., Wishart, D.S., and Xia, J. (2018). MetaboAnalyst 4.0: towards more transparent and integrative metabolomics analysis. Nucleic Acids Res. *46*, W486–W494.

Chong, J., Wishart, D.S., and Xia, J. (2019). Using MetaboAnalyst 4.0 for Comprehensive and Integrative Metabolomics Data Analysis. Curr. Protoc. Bioinforma. *68*.

Cingolani, P., Patel, V.M., Coon, M., Nguyen, T., Land, S.J., Ruden, D.M., and Lu, X. (2012). Using Drosophila melanogaster as a model for genotoxic chemical mutational studies with a new program, SnpSift. Front. Genet. *3*, 35.

Craigen, W.J. (1996). Leigh disease with deficiency of lipoamide dehydrogenase: Treatment failure with dichloroacetate. Pediatr. Neurol. *14*, 69–71.

Craven, L., Alston, C.L., Taylor, R.W., and Turnbull, D.M. (2017). Recent Advances in Mitochondrial Disease. Annu. Rev. Genomics Hum. Genet. *18*, 257–275.

Cui, Y., Chen, X., Luo, H., Fan, Z., Luo, J., He, S., Yue, H., Zhang, P., and Chen, R. (2016). BioCircos.js: An interactive Circos JavaScript library for biological data visualization on web applications. Bioinformatics *32*, 1740–1742.

Das, A.M., Steuerwald, U., and Illsinger, S. (2010). Inborn errors of energy metabolism associated with myopathies. J. Biomed. Biotechnol. *2010*.

Diez-Roux, G., Banfi, S., Sultan, M., Geffers, L., Anand, S., Rozado, D., Magen, A., Canidio, E., Pagani, M., Peluso, I., et al. (2011). A high-resolution anatomical atlas of the transcriptome in the mouse embryo. PLoS Biol. *9*, e1000582.

Elkabetz, Y., Panagiotakos, G., Al Shamy, G., Socci, N.D., Tabar, V., and Studer, L. (2008). Human ES cell-derived neural rosettes reveal a functionally distinct early neural stem cell stage. Genes Dev. *22*, 152–165.

Esterhuizen, K., van der Westhuizen, F.H., and Louw, R. (2017). Metabolomics of mitochondrial disease. Mitochondrion *35*, 97–110.

Fang, Q., Zhang, Y., Chen, X., Li, H., Cheng, L., Zhu, W., Zhang, Z., Tang, M., Liu, W., Wang, H., et al. (2020). Three-Dimensional Graphene Enhances Neural Stem Cell Proliferation Through Metabolic Regulation. Front. Bioeng. Biotechnol. *7*, 436.

Feeney, C.L., Lim, A.Z., Fagan, E., Blain, A., Bright, A., Maddison, J., Devine, H., Stewart, J., Taylor, R.W., Gorman, G.S., et al. (2019). A case-comparison study of pregnant women with mitochondrial disease – what to expect? BJOG An Int. J. Obstet. Gynaecol. *126*, 1380–1389.

Ferlin, T., Landrieu, P., Rambaud, C., Fernandez, H., Dumoulin, R., Rustin, P., and Mousson, B. (1997). Segregation of the G8993 mutant mitochondrial DNA through generations and embryonic tissues family at risk of Leigh syndrome. J. Pediatr. *131*, 447–449.

Ferrari, M., Jain, I.H., Goldberger, O., Rezoagli, E., Thoonen, R., Chen, K.-H., Sosnovik, D.E., Scherrer-Crosbie, M., Mootha, V.K., and Zapol, W.M. (2017). Hypoxia treatment reverses neurodegenerative disease in a mouse model of Leigh syndrome. Proc. Natl. Acad. Sci. *114*, E4241–E4250.

Ferreira, G.C., and McKenna, M.C. (2017). l-Carnitine and Acetyl-l-carnitine Roles and Neuroprotection in Developing Brain. Neurochem. Res. *42*, 1661–1675.

Finsterer, J. (2008). Leigh and Leigh-Like Syndrome in Children and Adults. Pediatr. Neurol. *39*, 223–235.

Florio, M., and Huttner, W.B. (2014). Neural progenitors, neurogenesis and the evolution of the neocortex. Development *141*, 2182–2194.

902 Galera-Monge, T., Zurita-Díaz, F., González-Páramos, C., Moreno-Izquierdo, A., Fraga, M.F.,
903 Fernández, A.F., Garesse, R., and Gallardo, M.E. (2016). Generation of a human iPSC line
904 from a patient with Leigh syndrome caused by a mutation in the MT-ATP6 gene. Stem Cell
905 Res. *16*, 766–769.
906 García-Cazorla, A., Oyarzabal, A., Fort, J., Robles, C., Castejón, E., Ruiz-Sala, P., Bodoy, S.,
907 Merinero, B., Lopez-Sala, A., Dopazo, J., et al. (2014). Two Novel Mutations in the BCKDK
908 (Branched-Chain Keto-Acid Dehydrogenase Kinase) Gene Are Responsible for a
909 Neurobehavioral Deficit in Two Pediatric Unrelated Patients. Hum. Mutat. *35*, 470–477.
910 Gerards, M., Sallevelt, S.C.E.H., and Smeets, H.J.M. (2016). Leigh syndrome: Resolving the
911 clinical and genetic heterogeneity paves the way for treatment options. Mol. Genet. Metab.
912 *117*, 300–312.
913 Gogos, J.A., Santha, M., Takacs, Z., Beck, K.D., Luine, V., Lucas, L.R., Nadler, J.V., and
914 Karayiorgou, M. (1999). The gene encoding proline dehydrogenase modulates
915 sensorimotor gating in mice. Nat. Genet. *21*, 434–439.
916 Gorman, G.S., Chinnery, P.F., DiMauro, S., Hirano, M., Koga, Y., McFarland, R., Suomalainen,
917 A., Thorburn, D.R., Zeviani, M., and Turnbull, D.M. (2016). Mitochondrial diseases. Nat.
918 Rev. Dis. Prim. *2*, 1–22.
919 Grace, H.E., Galdun, P., Lesnefsky, E.J., West, F.D., and Iyer, S. (2019). MRNA Reprogramming
920 of T8993G Leigh's Syndrome Fibroblast Cells to Create Induced Pluripotent Stem Cell
921 Models for Mitochondrial Disorders. Stem Cells Dev. *28*, 846–859.
922 Grier, J., Hirano, M., Karaa, A., Shepard, E., and Thompson, J.L.P. (2018). Diagnostic odyssey
923 of patients with mitochondrial disease Results of a survey. Neurol. Genet. *4*.
924 Harding, A.E., Holt, I.J., Sweeney, M.G., Brockington, M., and Davis, M.B. (1992). Prenatal
925 diagnosis of mitochondrial DNA8993 T→G disease. Am. J. Hum. Genet. *50*, 629–633.
926 Hattori, T., Hamazaki, T., Kudo, S., and Shintaku, H. (2016). Metabolic Signature of MELAS/Leigh
927 Overlap Syndrome in Patient-specific Induced Pluripotent Stem Cells Model. Osaka City
928 Med. J. *62*, 69–76.
929 Hinman, L.M., Sheu, K.-F.R., Baker, A.C., Kim, Y.T., and Blass, J.P. (1989). Deficiency of
930 pyruvate dehydrogenase complex (PDHC) in Leigh's disease fibroblasts: An abnormality
931 in lipoamide dehydrogenase affecting PDHC activation. Neurology *39*, 70–70.
932 Homem, C.C.F., Repic, M., and Knoblich, J.A. (2015). Proliferation control in neural stem and
933 progenitor cells. Nat. Rev. Neurosci. *16*, 647–659.
934 Hříbková, H., Grabiec, M., Klemová, D., Slaninová, I., and Sun, Y.-M. (2018). Five steps to form
935 neural rosettes: structure and function. J. Cell Sci. *131*, jcs206896.
936 Huh, T.L., Casazza, J.P., Huh, J.W., Chi, Y.T., and Song, B.J. (1990). Characterization of two
937 cDNA clones for pyruvate dehydrogenase E1β subunit and its regulation in tricarboxylic
938 acid cycle-deficient fibroblast. J. Biol. Chem. *265*, 13320–13326.
939 Inak, G., Lorenz, C., Lisowski, P., Zink, A., Mlody, B., and Prigione, A. (2017). Concise Review:
940 Induced Pluripotent Stem Cell-Based Drug Discovery for Mitochondrial Disease. Stem
941 Cells *35*, 1655–1662.
942 Inak, G., Rybak-Wolf, A., Lisowski, P., Juettner, R., Zink, A., Mlody, B., Glazar, P., Secker, C.,
943 Ciptasari, U.H., Stenzel, W., et al. (2019). SURF1 mutations causative of Leigh syndrome
944 impair human neurogenesis. BioRxiv 551390.
945 Itskovitz-Eldor, J., Schuldiner, M., Karsenti, D., Eden, A., Yanuka, O., Amit, M., Soreq, H., and
946 Benvenisty, N. (2000). Differentiation of Human Embryonic Stem Cells into Embryoid
947 Bodies Comprising the Three Embryonic Germ Layers. Mol. Med. *6*, 88–95.
948 Iyer, S., Bergquist, K., Young, K., Gnaiger, E., Rao, R.R., and Bennett, J.P. (2012). Mitochondrial
949 Gene Therapy Improves Respiration, Biogenesis, and Transcription in G11778A Leber's
950 Hereditary Optic Neuropathy and T8993G Leigh's Syndrome Cells. Hum. Gene Ther. *23*,
951 647–657.
952 Jain, I.H., Zazzeron, L., Goli, R., Alexa, K., Schatzman-Bone, S., Dhillon, H., Goldberger, O.,

Peng, J., Shalem, O., Sanjana, N.E., et al. (2016). Hypoxia as a therapy for mitochondrial disease. Science (80-.). *352*, 54–61.

Jain, I.H., Zazzeron, L., Goldberger, O., Marutani, E., Wojtkiewicz, G.R., Ast, T., Wang, H., Schleifer, G., Stepanova, A., Brepoels, K., et al. (2019). Leigh Syndrome Mouse Model Can Be Rescued by Interventions that Normalize Brain Hyperoxia, but Not HIF Activation. Cell Metab. *0*, 824-832.e3.

Jernberg, J.N., Bowman, C.E., Wolfgang, M.J., and Scafidi, S. (2017). Developmental regulation and localization of carnitine palmitoyltransferases (CPTs) in rat brain. J. Neurochem. *142*, 407–419.

Kelava, I., and Lancaster, M.A. (2016). Stem Cell Models of Human Brain Development. Cell Stem Cell *18*, 736–748.

Khacho, M., Clark, A., Svoboda, D.S., Azzi, J., MacLaurin, J.G., Meghaizel, C., Sesaki, H., Lagace, D.C., Germain, M., Harper, M.E., et al. (2016). Mitochondrial Dynamics Impacts Stem Cell Identity and Fate Decisions by Regulating a Nuclear Transcriptional Program. Cell Stem Cell.

Lake, N.J., Bird, M.J., Isohanni, P., and Paetau, A. (2015). Leigh syndrome: neuropathology and pathogenesis. J. Neuropathol. Exp. Neurol. *74*, 482–492.

Lake, N.J., Compton, A.G., Rahman, S., and Thorburn, D.R. (2016). Leigh syndrome: One disorder, more than 75 monogenic causes. Ann. Neurol. *79*, 190–203.

Lancaster, M.A., and Knoblich, J.A. (2014). Generation of cerebral organoids from human pluripotent stem cells. Nat. Protoc. *9*, 2329–2340.

Lancaster, M.A., Corsini, N.S., Wolfinger, S., Gustafson, E.H., Phillips, A.W., Burkard, T.R., Otani, T., Livesey, F.J., and Knoblich, J.A. (2017). Guided self-organization and cortical plate formation in human brain organoids. Nat. Publ. Gr. *35*.

Leigh, D. (1951). Subacute necrotizing encephalomyelopathy in an infant. J. Neurol. Neurosurg. Psychiatry *14*, 216–221.

Lorenz, C., Lesimple, P., Bukowiecki, R., Zink, A., Inak, G., Mlody, B., Singh, M., Semtner, M., Mah, N., Auré, K., et al. (2017). Human iPSC-Derived Neural Progenitors Are an Effective Drug Discovery Model for Neurological mtDNA Disorders. Cell Stem Cell *20*, 659-674.e9.

Lui, J.H., Hansen, D. V., and Kriegstein, A.R. (2011). Development and evolution of the human neocortex. Cell *146*, 18–36.

Di Lullo, E., and Kriegstein, A.R. (2017). The use of brain organoids to investigate neural development and disease. Nat. Rev. Neurosci. *18*, 573–584.

Ma, H., Folmes, C.D.L., Wu, J., Morey, R., Mora-Castilla, S., Ocampo, A., Ma, L., Poulton, J., Wang, X., Ahmed, R., et al. (2015). Metabolic rescue in pluripotent cells from patients with mtDNA disease. Nature *524*, 234–238.

Manoli, I., and Venditti, C.P. (2016). Disorders of branched chain amino acid metabolism. Transl. Sci. Rare Dis. *1*, 91–110.

Mathieu, J., and Ruohola-Baker, H. (2017). Metabolic remodeling during the loss and acquisition of pluripotency. Dev. *144*, 541–551.

Medelnik, J.-P., Roensch, K., Okawa, S., del Sol, A., Chara, O., Mchedlishvili, L., and Tanaka, E.M. (2018). Signaling-Dependent Control of Apical Membrane Size and Self-Renewal in Rosette-Stage Human Neuroepithelial Stem Cells. Stem Cell Reports *10*, 1751–1765.

Di Meo, I., Marchet, S., Lamperti, C., Zeviani, M., and Viscomi, C. (2017). AAV9-based gene therapy partially ameliorates the clinical phenotype of a mouse model of Leigh syndrome. Gene Ther. *24*, 661–667.

Miyabayashi, S., Ito, T., Narisawa, K., Iinuma, K., and Tada, K. (1985). Biochemical study in 28 children with lactic acidosis, in relation to Leigh's encephalomyelopathy. Eur. J. Pediatr. *143*, 278–283.

Müller, F.J., Schuldt, B.M., Williams, R., Mason, D., Altun, G., Papapetrou, E.P., Danner, S., Goldmann, J.E., Herbst, A., Schmidt, N.O., et al. (2011). A bioinformatic assay for

pluripotency in human cells. Nat. Methods *8*, 315–317.

Muratore, C.R., Srikanth, P., Callahan, D.G., and Young-Pearse, T.L. (2014). Comparison and optimization of hiPSC forebrain cortical differentiation protocols. PLoS One *9*, e105807.

Nakano, C., Takashima, S., and Takeshita, K. (1989). Carnitine concentration during the development of human tissues. Early Hum. Dev. *19*, 21–27.

Nesbitt, V., Alston, C.L., Blakely, E.L., Fratter, C., Feeney, C.L., Poulton, J., Brown, G.K., Turnbull, D.M., Taylor, R.W., and McFarland, R. (2014). A national perspective on prenatal testing for mitochondrial disease. Eur. J. Hum. Genet. *22*, 1255–1259.

Oshida, K., Shimizu, T., Takase, M., Tamura, Y., Shimizu, T., and Yamashiro, Y. (2003). Effects of dietary sphingomyelin on central nervous system myelination in developing rats. Pediatr. Res. *53*, 589–593.

Pampaloni, F., Reynaud, E.G., and Stelzer, E.H.K. (2007). The third dimension bridges the gap between cell culture and live tissue. Nat. Rev. Mol. Cell Biol. *8*, 839–845.

Panopoulos, A.D., Yanes, O., Ruiz, S., Kida, Y.S., Diep, D., Tautenhahn, R., Herrerías, A., Batchelder, E.M., Plongthongkum, N., Lutz, M., et al. (2012). The metabolome of induced pluripotent stem cells reveals metabolic changes occurring in somatic cell reprogramming. Cell Res. *22*, 168–177.

Parikh, S., Goldstein, A., Karaa, A., Koenig, M.K., Anselm, I., Brunel-Guitton, C., Christodoulou, J., Cohen, B.H., Dimmock, D., Enns, G.M., et al. (2017). Patient care standards for primary mitochondrial disease: A consensus statement from the mitochondrial medicine society. Genet. Med. *19*, 1–18.

Paşca, A.M., Sloan, S.A., Clarke, L.E., Tian, Y., Makinson, C.D., Huber, N., Kim, C.H., Park, J.-Y., O'Rourke, N.A., Nguyen, K.D., et al. (2015). Functional cortical neurons and astrocytes from human pluripotent stem cells in 3D culture. Nat Methods. *12*, 671–678.

Pastores, G.M., Santorelli, F.M., Shanske, S., Gelb, B.D., Fyfe, B., Wolfe, D., and Willner, J.P. (1994). Leigh syndrome and hypertrophic cardiomyopathy in an infant with a mitochondrial DNA point mutation (T8993G). Am. J. Med. Genet. *50*, 265–271.

Quadrato, G., Brown, J., and Arlotta, P. (2016). The promises and challenges of human brain organoids as models of neuropsychiatric disease. Nat. Med. *22*, 1220–1228.

Rahman, J., and Rahman, S. (2018). Mitochondrial medicine in the omics era. Lancet *391*, 2560–2574.

Rasmussen, M.L., and Gama, V. (2020). A connection in life and death: The BCL-2 family coordinates mitochondrial network dynamics and stem cell fate. In International Review of Cell and Molecular Biology, (Elsevier Inc.), p.

Rastogi, A., Joshi, P., Contreras, E., and Gama, V. (2019). Remodeling of mitochondrial morphology and function: an emerging hallmark of cellular reprogramming. Cell Stress *3*, 181–194.

Rema, V., Bali, K.K., Ramachandra, R., Chugh, M., Darokhan, Z., and Chaudhary, R. (2008). Cytidine-5-diphosphocholine supplement in early life induces stable increase in dendritic complexity of neurons in the somatosensory cortex of adult rats. Neuroscience *155*, 556–564.

Robel, S., Mori, T., Zoubaa, S., Schlegel, J., Sirko, S., Faissner, A., Goebbels, S., Dimou, L., and Götz, M. (2009). Conditional deletion of β1-integrin in astroglia causes partial reactive gliosis. Glia *57*, 1630–1647.

Robel, S., Berninger, B., and Götz, M. (2011). The stem cell potential of glia: Lessons from reactive gliosis. Nat. Rev. Neurosci. *12*, 88–104.

Romero-Morales, A.I., O'Grady, B.J., Balotin, K.M., Bellan, L.M., Lippmann, E.S., and Gama, V. (2019). Spin∞ an improved miniaturized spinning bioreactor for the generation of human cerebral organoids from pluripotent stem cells. BioRxiv 687095.

Saito, T., Hanai, S., Takashima, S., Nakagawa, E., Okazaki, S., Inoue, T., Miyata, R., Hoshino, K., Akashi, T., Sasaki, M., et al. (2011). Neocortical layer formation of human developing

brains and lissencephalies: Consideration of layer-specific marker expression. Cereb. Cortex *21*, 588–596.

Schaefer, A., Lim, A., and Gorman, G. (2019). Epidemiology of Mitochondrial Disease. In Diagnosis and Management of Mitochondrial Disorders, (Cham: Springer International Publishing), pp. 63–79.

Schubert, M.B., and Vilarinho, L. (2020). Molecular basis of Leigh syndrome: A current look. Orphanet J. Rare Dis. *15*, 1–14.

Shaheen, R., Han, L., Faqeih, E., Ewida, N., Alobeid, E., Phizicky, E.M., and Alkuraya, F.S. (2016). A homozygous truncating mutation in PUS3 expands the role of tRNA modification in normal cognition. Hum. Genet. *135*, 707–713.

Song, C., Xu, F., Ren, Z., Zhang, Y., Meng, Y., Yang, Y., Lingadahalli, S., Cheung, E., Li, G., Liu, W., et al. (2019). Elevated Exogenous Pyruvate Potentiates Mesodermal Differentiation through Metabolic Modulation and AMPK/mTOR Pathway in Human Embryonic Stem Cells. Stem Cell Reports *13*, 338–351.

Sorbi, S., and Blass, J.P. (1982). Abnormal acfivafion of pyruvate dehydrogenase in Leigh disease fibroblasts. Neurology *32*, 555–558.

Steffann, J., Gigarel, N., Corcos, J., Bonnière, M., Encha-Razavi, F., Sinico, M., Prevot, S., Dumez, Y., Yamgnane, A., Frydman, R., et al. (2007). Stability of the m.8993T→G mtDNA mutation load during human embryofetal development has implications for the feasibility of prenatal diagnosis in NARP syndrome. J. Med. Genet. *44*, 664–669.

Stern, H.J. (1994). Lactic acidosis in paediatrics: Clinical and laboratory evaluation. Ann. Clin. Biochem. *31*, 410–419.

Takahashi, K., Tanabe, K., Ohnuki, M., Narita, M., Ichisaka, T., Tomoda, K., and Yamanaka, S. (2007). Induction of Pluripotent Stem Cells from Adult Human Fibroblasts by Defined Factors. Cell *131*, 861–872.

TCW, J., Wang, M., Pimenova, A.A., Bowles, K.R., Hartley, B.J., Lacin, E., Machlovi, S.I., Abdelaal, R., Karch, C.M., Phatnani, H., et al. (2017). An Efficient Platform for Astrocyte Differentiation from Human Induced Pluripotent Stem Cells. Stem Cell Reports *9*, 600–614.

The International Stem Cell Initiative (2018). Assessment of established techniques to determine developmental and malignant potential of human pluripotent stem cells. Nat. Commun. *9*, 1925.

Tibbitt, M.W., and Anseth, K.S. (2012). Dynamic microenvironments: The fourth dimension. Sci. Transl. Med. *4*, 160ps24-160ps24.

Uittenbogaard, M., Brantner, C.A., Fang, Z.S., Wong, L.J.C., Gropman, A., and Chiaramello, A. (2018). Novel insights into the functional metabolic impact of an apparent de novo m.8993T>G variant in the MT-ATP6 gene associated with maternally inherited form of Leigh Syndrome. Mol. Genet. Metab. *124*, 71–81.

Vescovi, A.L., and Snyder, E.Y. (1999). Establishment and properties of neural stem cell clones: Plasticity in vitro and in vivo. In Brain Pathology, (International Society of Neuropathology), pp. 569–598.

Vorstman, J.A.S., Turetsky, B.I., Sijmens-Morcus, M.E.J., De Sain, M.G., Dorland, B., Sprong, M., Rappaport, E.F., Beemer, F.A., Emanuel, B.S., Kahn, R.S., et al. (2009). Proline affects brain function in 22q11DS children with the low activity COMT158 allele. Neuropsychopharmacology *34*, 739–746.

White, S.L., Collins, V.R., Wolfe, R., Cleary, M.A., Shanske, S., DiMauro, S., Dahl, H.H.M., and Thorburn, D.R. (1999). Genetic counseling and prenatal diagnosis for the mitochondrial DNA mutations at nucleotide 8993. Am. J. Hum. Genet. *65*, 474–482.

Wilson, P.G., and Stice, S.S. (2006). Development and differentiation of neural rosettes derived from human embryonic stem cells. Stem Cell Rev. *2*, 67–77.

Wu, J., Ocampo, A., and Belmonte, J.C.I. (2016). Cellular Metabolism and Induced Pluripotency. Cell *166*, 1371–1385.

1106 Xia, J., and Wishart, D.S. (2010). MetPA: a web-based metabolomics tool for pathway analysis
1107 and visualization. Bioinformatics *26*, 2342–2344.
1108 Xia, J., and Wishart, D.S. (2011a). Metabolomic data processing, analysis, and interpretation
1109 using MetaboAnalyst. Curr. Protoc. Bioinforma. *34*, 1–48.
1110 Xia, J., and Wishart, D.S. (2011b). Web-based inference of biological patterns, functions and
1111 pathways from metabolomic data using MetaboAnalyst. Nat. Protoc. *6*, 743–760.
1112 Xia, J., Psychogios, N., Young, N., and Wishart, D.S. (2009). MetaboAnalyst: a web server for
1113 metabolomic data analysis and interpretation. Nucleic Acids Res. *37*, W652–W660.
1114 Zanotelli, M.R., Goldblatt, Z.E., Miller, J.P., Bordeleau, F., Li, J., VanderBurgh, J.A., Lampi, M.C.,
1115 King, M.R., and Reinhart-King, C.A. (2018). Regulation of ATP utilization during metastatic
1116 cell migration by collagen architecture. Mol. Biol. Cell *29*, 1–9.
1117 Zanotelli, M.R., Rahman-Zaman, A., VanderBurgh, J.A., Taufalele, P. V., Jain, A., Erickson, D.,
1118 Bordeleau, F., and Reinhart-King, C.A. (2019). Energetic costs regulated by cell mechanics
1119 and confinement are predictive of migration path during decision-making. Nat. Commun.
1120 *10*, 1–12.
1121 Zeisel, S.H. (2006). The fetal origins of memory: The role of dietary choline in optimal brain
1122 development. J. Pediatr. *149*, S131–S136.
1123 Zeisel, S.H., and Niculescu, M.D. (2006). Perinatal Choline Influences Brain Structure and
1124 Function. Nutr. Rev. *64*, 197–203.
1125 Zhang, S.-C., Wernig, M., Duncan, I.D., Brüstle, O., and Thomson, J.A. (2001). In vitro
1126 differentiation of transplantable neural precursors from human embryonic stem cells. Nat.
1127 Biotechnol. *19*, 1129–1133.
1128

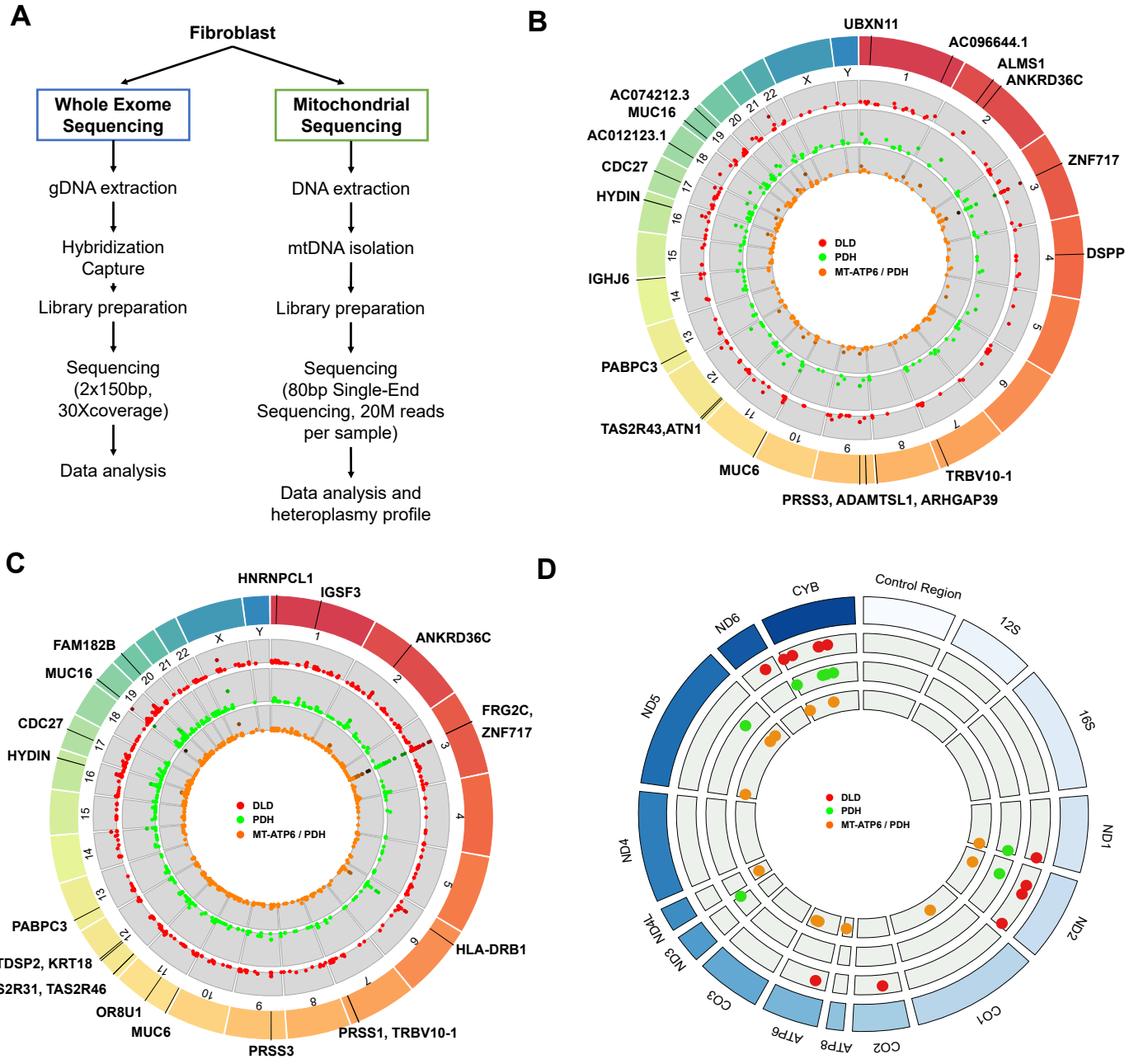

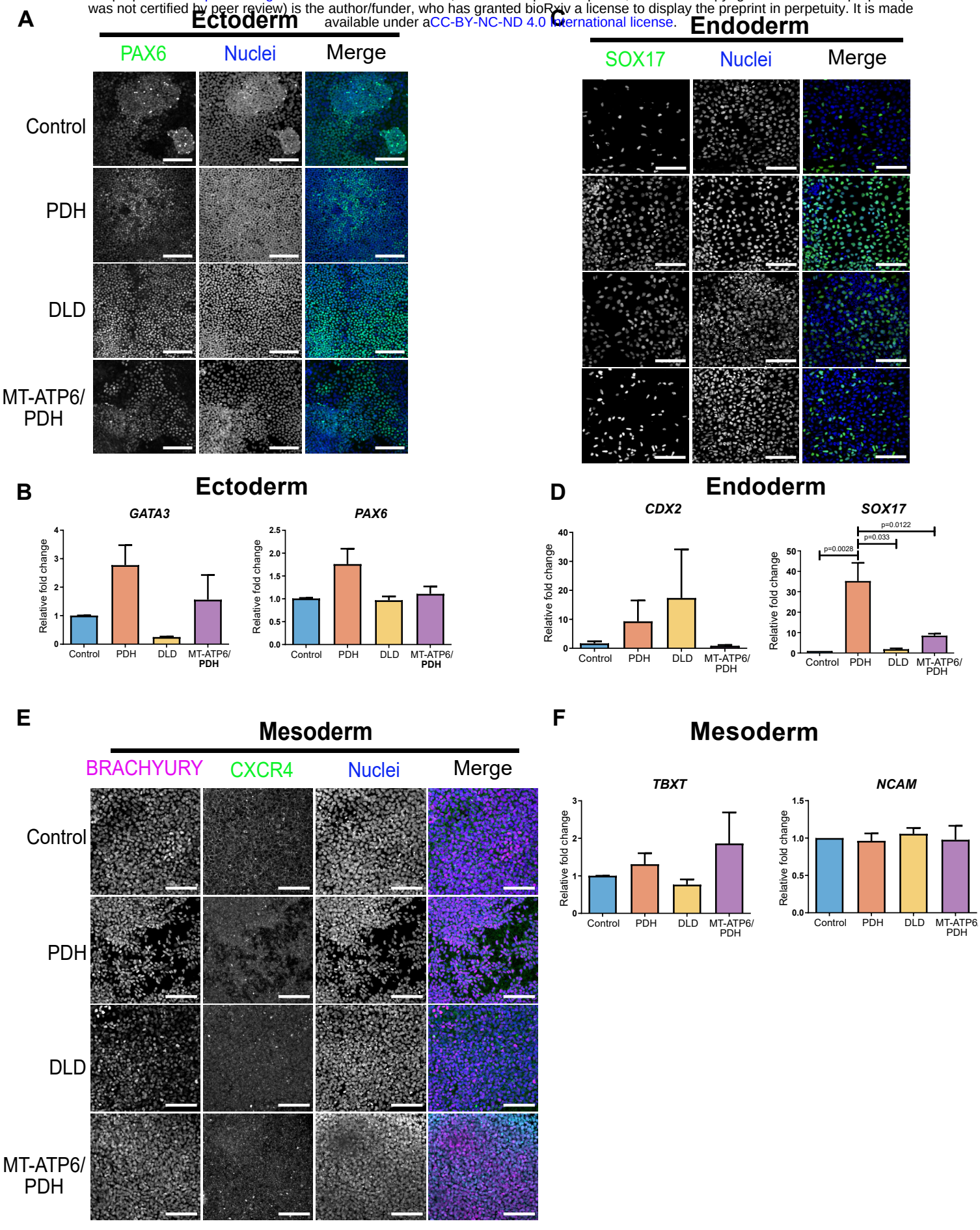

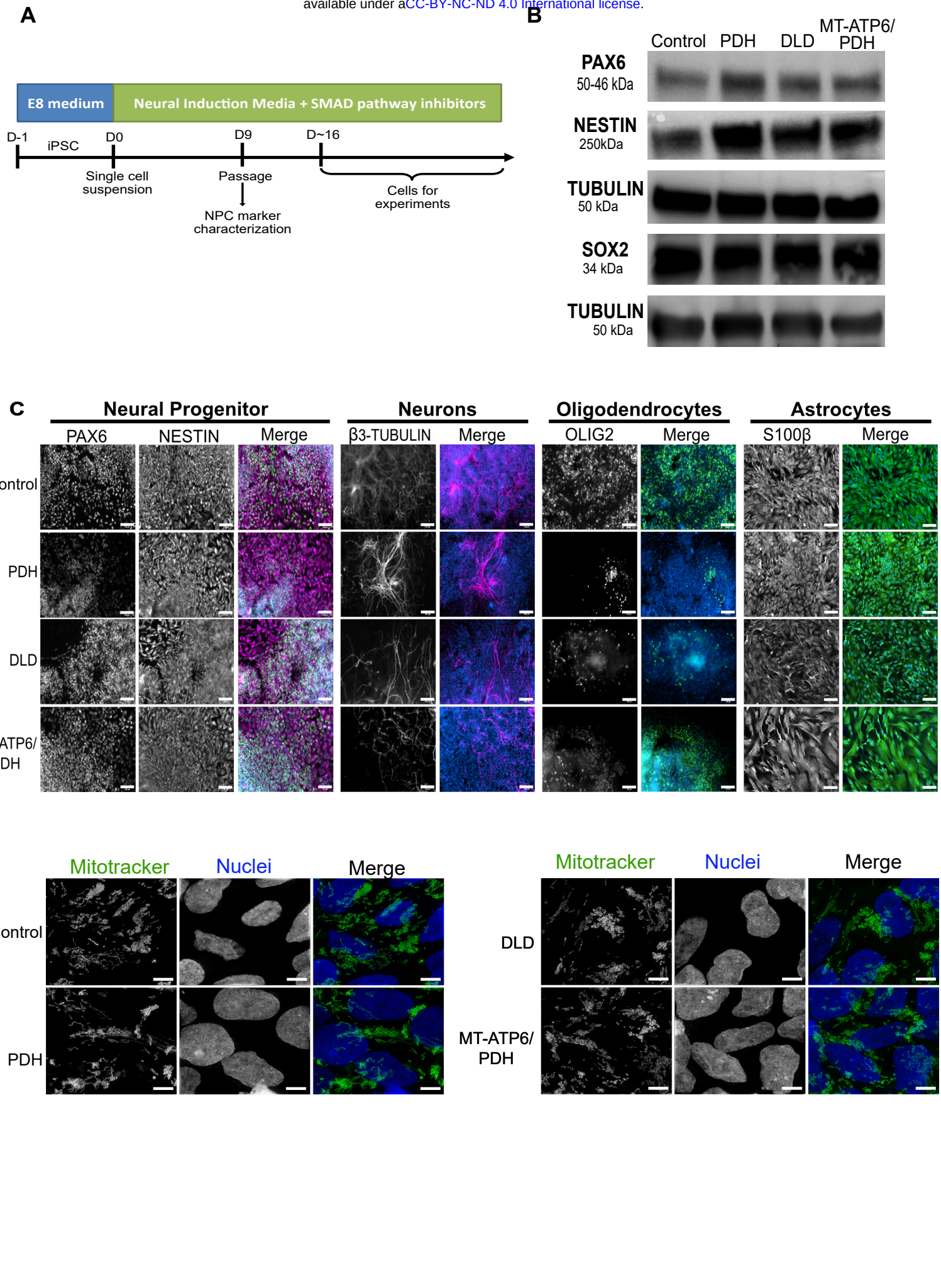

A

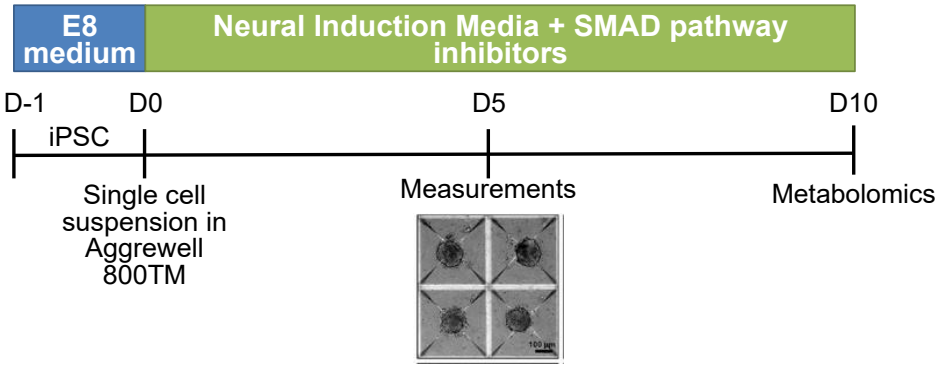

B

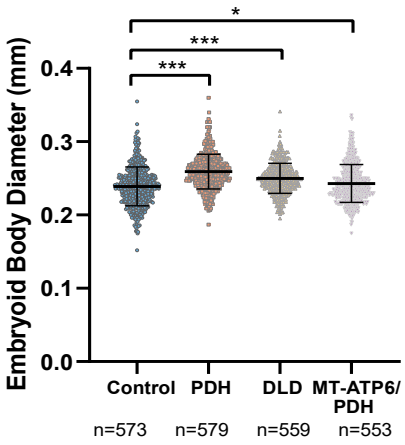

C

Pathway	Hits	Total	Raw p	-log(p)	Holm adjust	FDR	Impact
Alanine, aspartate and glutamate metabolism	16	28	9.88E-13	27.643	8.30E-11	8.30E-11	0.76282
Synthesis and degradation of ketone bodies	1	5	0.29616	1.2169	1	0.85783	0.6
Arginine biosynthesis	9	14	3.24E-08	17.244	2.69E-06	1.36E-06	0.5736
Glycine, serine and threonine metabolism	8	33	0.001137	6.7797	0.088659	0.01364	0.55868
D-Glutamine and D-glutamate metabolism	3	6	0.005201	5.259	0.38485	0.036405	0.5
Cysteine and methionine metabolism	9	33	0.000209	8.4735	0.016923	0.003721	0.47436
Nicotinate and nicotinamide metabolism	4	15	0.015176	4.188	1	0.091058	0.42895
Beta-Alanine metabolism	2	21	0.42186	0.86309	1	1	0.39925
Pyrimidine metabolism	14	39	6.64E-08	16.527	5.45E-06	1.86E-06	0.32533
Arginine and proline metabolism	8	38	0.00301	5.806	0.22873	0.028089	0.28068
Citrate cycle (TCA cycle)	6	20	0.001488	6.5105	0.11456	0.015622	0.27512
Pentose phosphate pathway	3	22	0.18299	1.6984	1	0.61483	0.27226
Purine metabolism	12	65	0.000959	6.9499	0.075743	0.013423	0.27171
Tyrosine metabolism	7	42	0.02008	3.908	1	0.11245	0.2369
Pyruvate metabolism	3	22	0.18299	1.6984	1	0.61483	0.20684
Glycolysis / Gluconeogenesis	3	26	0.25592	1.3629	1	0.7962	0.20594
Glyoxylate and dicarboxylate metabolism	7	32	0.004395	5.4272	0.32966	0.036405	0.20371

A

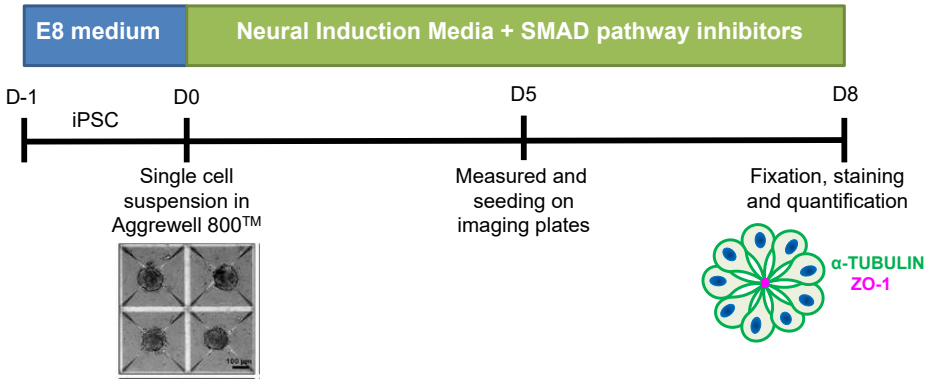

B

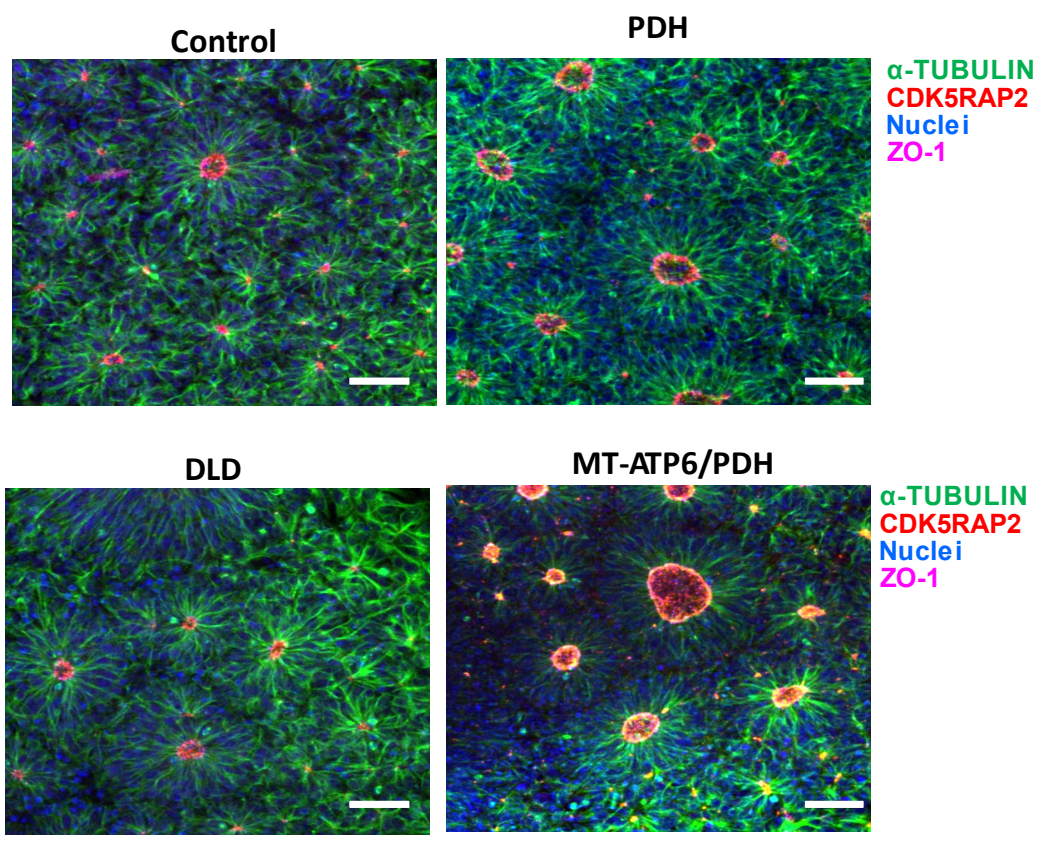

C

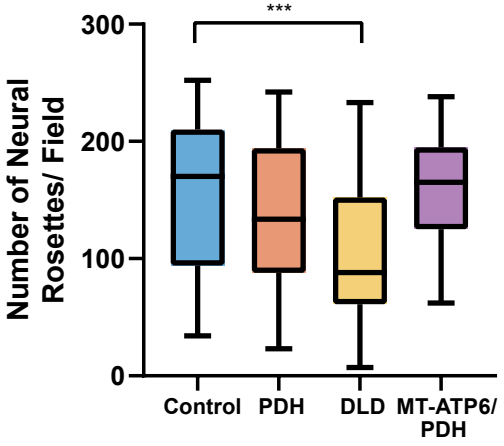

D